Geophysical Journal International

Geophys. J. Int. (2011) **184,** 416–438 doi: 10.1111/j.1365-246X.2010.04847.x

Upper-mantle structures beneath USArray derived from waveform complexity

Daoyuan Sun[1] and Don Helmberger[2]

[1] *Department of Terrestrial Magnetism, Carnegie Institution of Washington, Washington,* DC 20015, *USA. E-mail: dsun@dtm.ciw.edu*
[2] *Seismological Laboratory, California Institute of Technology, Pasadena,* CA 91125, *USA*

Accepted 2010 October 11. Received 2010 September 30; in original form 2010 April 19

SUMMARY

Tomographic imaging of the crust and upper mantle beneath the western United States has greatly improved with the addition of USArray data. These models display many detailed images of both fast and slow blobs penetrating into the transition zone. To study such features, we apply a newly developed technique, called MultiPath Detector analysis, to the SH waveform data. The method simulates each observed body waveform by performing a decomposition; by $[S(t) + C \times S(t - \Delta_{LR})]/2$, where $S(t)$ is the synthetics for a reference model. Time separation Δ_{LR} and amplitude ratio C are needed to obtain a high cross-correlation between a simulated waveform and data. The travel time of the composite waveform relative to the reference model synthetics is defined as Δ_T. A simulated annealing algorithm is used to determine the parameters Δ_{LR} and C. We also record the amplitude ratio (Amp) between the synthetics for the reference model relative to the data. Generally, large Δ_{LR} values are associated with low Amp's. Whereas the conventional tomography yields a travel time correction (Δ_T), our analysis yields an extra parameter (Δ_{LR}), which describes the waveform complexity. With the array, we can construct a mapping of the gradient of Δ_{LR} with complexity patterns. A horizontal structure introduces waveform complexity along the distance profile (in-plane multipathing). An azimuthally orientation Δ_{LR} pattern indicates a vertical structure with out-of-plane multipathing. Using such maps generated from artificial data, we can easily recognize features produced by dipping fast structures and slow structures (DSS). Many of these features display organized waveform complexity that are distinctly directional indicative of dipping sharp-edges. Here, we process the array data for events arriving from various azimuths and construct maps of multipathing patterns. The similarity between tomographic features and complexity maps is striking. When features are dipping such as the slab structures beneath the Cascade Range and Nevada, strong complexity is observed from Southeastern events arriving along these ray paths with split pulses separated up to 6 s for both. This requires extended slab segments to at least 600/300 km with a 4/8 per cent velocity jump along the edges. One of the most dramatic set of DSS observations is associated with a slow northwest dipping conduit beneath Yellowstone that extends into the transition zone. A number of forward modelling experiments are included for the strongest patterns formed by sharpening present tomographic images.

Key words: Body waves; Dynamics of lithosphere and mantle.

1 INTRODUCTION

Recent updates of western United States (WUS) upper-mantle structure (Roth *et al.* 2008; Yang *et al.* 2008) have sharpened some of the features determined earlier by the many PASSCAL experiments (Humphreys & Dueker 1994). For example, the *P*-wave tomographic model by Burdick *et al.* (2008, 2009) clearly displays the relatively slow western basin-and-range (BR) province including all of Nevada and much of Arizona at depths of 100 km (Fig. 1). Significant strips of slow velocity along the Snake River Plain (SRP) structure, the St. George lineament and Rio Grande Rift (RGR) structure are detailed. Most of these features are weak at depths greater than 400 km suggesting relatively shallow mantle involvement in crustal tectonic features (Karlstrom *et al.* 2005). Patches of slow velocities are interpreted in terms of warm conditions involving fluids released by the earlier flat Fallon Plate as it moved into the transition zone (Humphreys *et al.* 2003). It appears that tomography works reasonably well for shallow patch features less than 300 km, in that arrivals from most azimuths sample the structure roughly along the 1-D reference paths. However, in some recent studies (Song & Helmberger 2007a,b,c), demonstrate that teleseismic waveform data is highly azimuthally dependent. Arrivals from the northwest (NW)

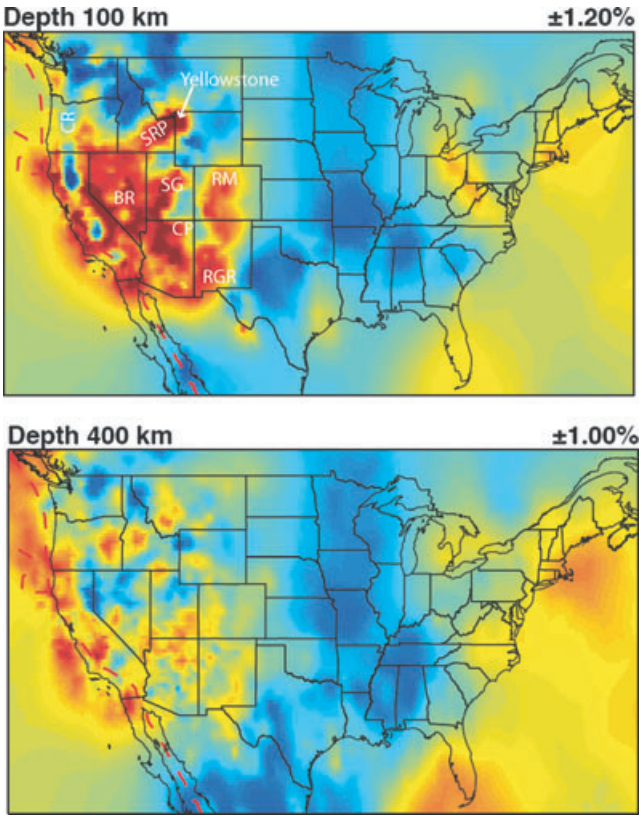

Figure 1. The *P*-wave tomographic model beneath WUS, revised after Burdick *et al.* (2009). It clearly displays the relatively slow western Basin and Range including Nevada and most of Arizona at depth down to 200 km. Significant strips of slow velocities along the Snake River Plain (SRP) structure, the St. George lineament (SG) and the Rio Grande Rift (RGR) are detailed. Most of the features are gone at depth greater than 300 km suggesting relatively shallow mantle structure involvement in crustal tectonic feature. However, to model multipathing generally requires deeper structures. The other principal geological features are marked, including Yellowstone, the Cascade Range (CR), the Rock Mountain (RM) and the Colorado Plateau (CP).

as recorded on the La Ristra array are relatively simple and uniform in shape with *P*-waves showing 1.5 s delay relative to IASPEI and *S*-waves about 2 s (Gao *et al.* 2004). Events from the southeast (SE) display a great deal of complexity. This feature is also observed in USArray data, Fig. 2 for all events arriving along this particular azimuth.

The normalized waveforms are given in Fig. 2(a) with true amplitudes displayed in Fig. 2(d). An azimuthal record section along line AA′ is shown in Fig. 2(b) with the upper half sampling the relatively slow paths and jumping to the fast paths to the northeast. The changeover is near station X22A (top left corner in Fig. 2d) with a simple strong arrival, with multipathing to the south. We chose a deep event (20080903) to allow a clear view of ScS. Generally, the complexity in ScS is similar to that in S but because the structure is 3-D and the cross-section is near a boundary, we observe considerable variation, that is, the station pair 118A and 219A. Note the jump of 5 s in differential (ScS-S) travel times over a distance change of less than 100 km. Such features occur for deep mantle structures where we have introduced a multipath detector (MPD) where Δ_{LR} is a measure of complexity, with large values associated with the largest split pulses. For example, note the correlation of complex waveforms with the pink zones in Fig. 2(d). As displayed in Song & Helmberger (2007a), events from the NW do not show such patterns while events from South America consistently have such features.

The geometry of the La Ristra array was configurated to cross significant structure while being aligned with the primary source of events, mainly, the north Pacific and South America with their deep seismicity. Much of the strongest evidence for complexity occurs along these two azimuths where the 2-D tomographic models are the best resolved. In Fig. 3, we present cross-sections from some current tomographic models along the same profile across WUS. The XA model (Xue & Allen 2010) has the strongest linear dipping strips. BK model (Burdick *et al.* 2008) has the most data since it includes the International Seismological Centre (ISC) travel time picks. SCH model (Schmandt *et al.* 2009; Schmandt & Humphreys 2010a,b) includes the data used by Gao *et al.* (2004) and appears quite similar with the fast dipping structure near the New Mexico-Texas boundary. Two *S*-wave tomography models are represented in Fig. 3, including a comparison of SH for the Schmandt and Humphreys model and a multiple frequency SH model (Tian) from Tian *et al.* (2009). The former is similar to the Gao *et al.* (2003) model for the New Mexico structure. Synthetics generated from the 2-D tomographic model presented by Gao *et al.* (2003) display some broadening of the records at stations near the pink zone in Fig. 2(d), but not enough to produce the multipathing. Song & Helmberger (2007a,b) explain this multipathing by simply enhancing the existing model. The data can also be modelled by replacing the elongated high velocity strip beneath the southern profile by a uniform slab, 120 km thick, 4 per cent velocity increase and dipping 70–75° to the SE to about 600 km. The *P*-velocity increase is slightly less indicating a scale factor (R) of $\mathrm{d}\ln V_s/\mathrm{d}\ln V_p \cong 1.25$. This low value compared to (1.5 to 2) derived from the HiNet study (Chen *et al.* 2007) suggests a drip of continental lithosphere falling into the mantle (Song & Helmberger 2007c).

The Tian model has a stronger slow zone beneath the Colorado Plateau, which helps explain its elevation. This model is similar to the SCH model but addresses many issues involved in better matching waveform data and uses the amplitude data as well (Sigloch *et al.* 2006, 2008). Many of the amplitude issues along the La Ristra array are addressed in their paper along with the issues causing a breakdown in ray-theory when the travel time jumps reach one quarter of the wave period, as displayed in Fig. 2(d).

Although the models in Fig. 3 appear quite different, they clearly show the dipping Juan de Fuca slab structure penetrating into the upper mantle. A deeper structure beneath northernmost Nevada is also apparent in all these models. There are a number of ways to validate these models and to make them look more like distinct-continuous structures; one is to generate synthetic seismograms from these models and compare with record sections such as displayed in Fig. 4 or perhaps just the first arrivals such as presented by Song & Helmberger (2007a,b,c) or extended wave train by Chen *et al.* (2007) in 2-D and 3-D.

Still another approach is to process the array data to better exploit the array wavefield coverage. To accomplish this, we process the waveforms of neighbouring stations to better capture the nature of the observations similar to the technique introduced by Sun *et al.* (2009). The basic approach is to treat every arrival in terms of its waveshape and idealize it as constructed from a Fresnel zone. In particular, each pulse samples a bundle of ray paths, which can be in constructive or destructive interference (Helmberger & Ni 2005). For example, if paths sample each side of a slab boundary with differences in timing comparable to the source duration, they are expected to split and cause multipathing as apparently happens at the shaded stations given in Fig. 4. Furthermore, if an individual

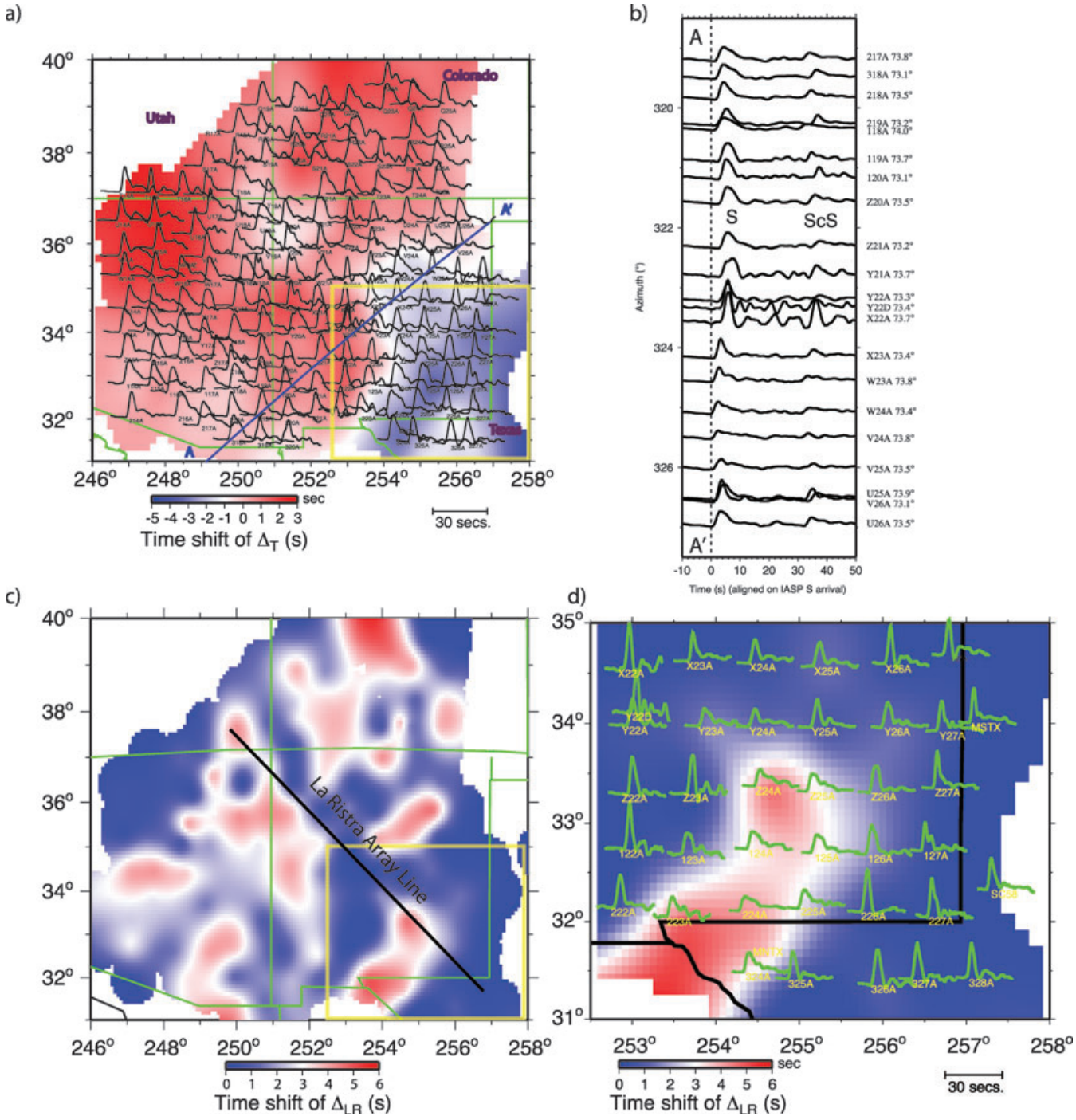

Figure 2. (a) USArray records (direct S) for the South American event 20080903. Some waveforms are simple and some are strongly distorted, which indicates the occurrence of strong multipathing and upper-mantle structure. All the waveforms in (a) are scaled to the same amplitude. The records along profile AA′ are plotted in (b). For two very close stations around azimuth of 320°, station 219A show simple S and ScS waveform, but station 118A displays waveform distortions on both phases. The MPD pattern of Δ_{LR} is displayed in (c). The Δ_{LR} is a measure of complexity, with large values associated with the largest split pulses. Note that complex waveforms are directly associated with low amplitude as in (d).

observation is complicated, its nearest neighbour should be influenced in a related fashion depending on the geometry and density of stations.

In the next section, we examine the complexity of S and sS in terms of modelling and introduce some complexity measuring tools. Then, we process USArray data (see Table 1) to create maps of diffractions from some of the most significant structures with a sprinkling of forward modelling.

2 METHODOLOGY

It is generally assumed that body wave pulses are simple enough to apply cross-correlation techniques in measuring traveltimes and that ray paths from a reference model can be held constant. Tomography is then applied to map-out small changes in a checkerboard to satisfy the traveltimes. In this section, we will introduce an alternative method for analysing records used earlier in studying deep mantle

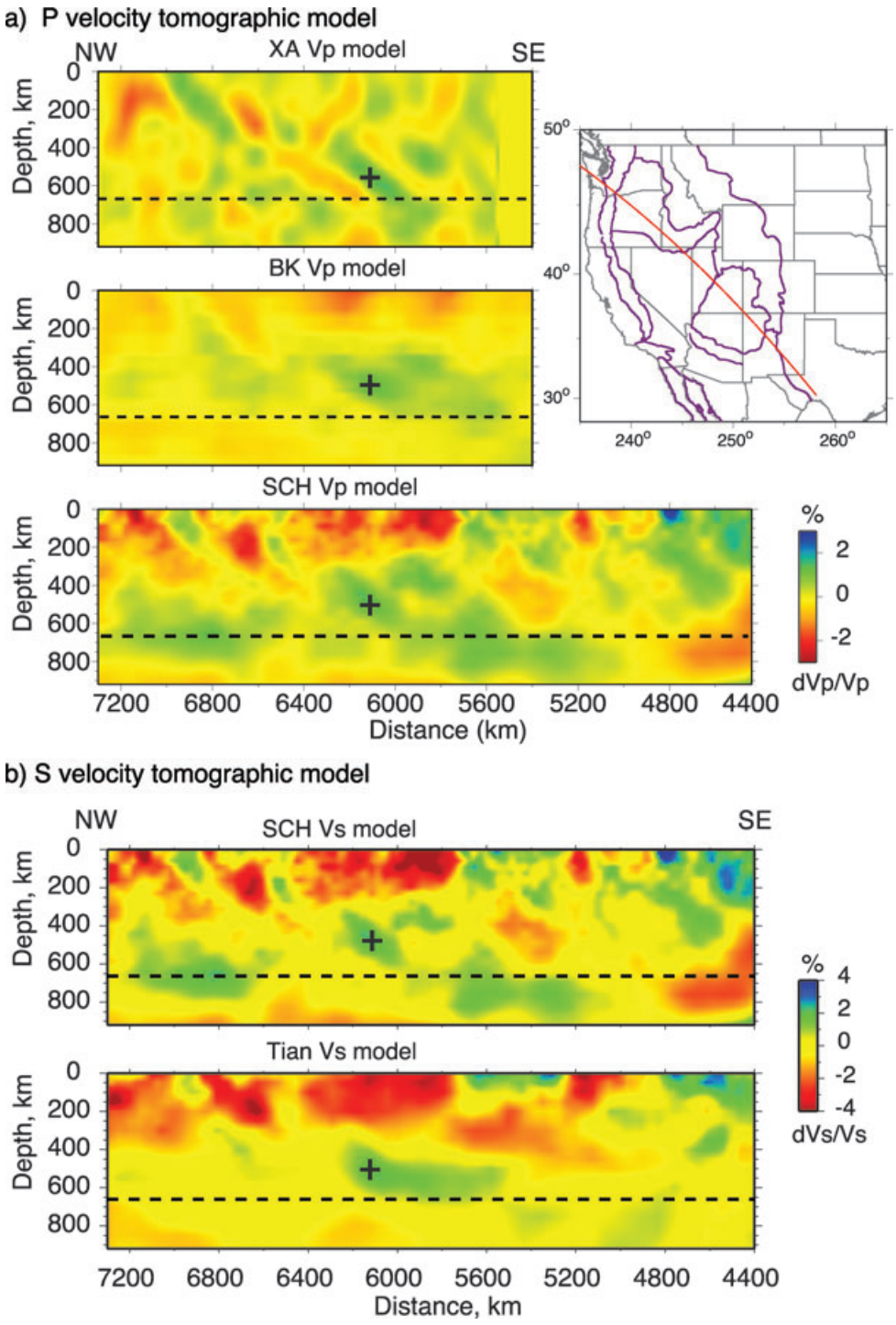

Figure 3. Comparison between different (a) P and (b) S tomographic models across WUS along profile denoted on the right. XA model: (Xue & Allen 2010); BK model (Burdick *et al.* 2008); SCH model (Schmandt & Humphreys 2010a); Tian model (Tian *et al.* 2009). Although different models display comparable features, they are very different in details, which are controlled by different methods and data set used in the inversions.

phases (Sun *et al.* 2009) that is more sensitive to lateral gradients in velocity. However, we will begin by conducting a validation-type study on one of the models presented in Fig. 3, namely, the model by Xue & Allen (2010).

2.1 Validation by 2-D modelling

We use the finite-difference (FD) code discussed in Song & Helmberger (2007a) which allows for shear-dislocation sources. The grid spacing and time stepping is the same where we only update the grid near the wave front of interest (Vidale 1988). Synthetics can then be generated for these cross-sections in 2-D. Although the model with velocity anomalies as inflated by 2.5 works quite well in predicting the SH observations from Fig. 3, we attempted to strip out small structures and enhance those features that produced the multipathing. An example model is presented in Fig. 5 along with fits to timing, amplitudes and waveform comparisons. We have included some ray paths indicating at what distances these structures

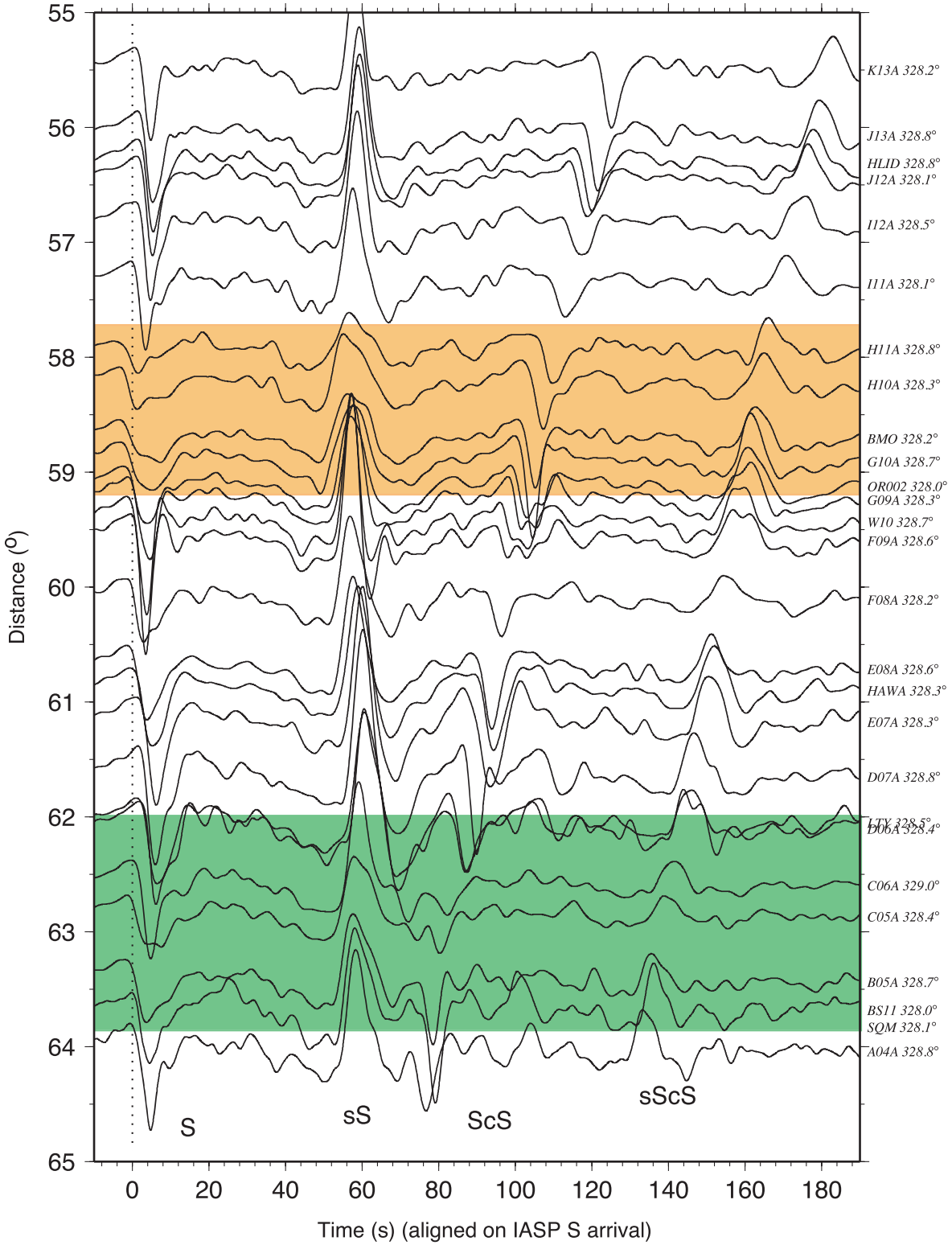

Figure 4. Observed waveform data from stations at northwestern US for a South American event (20071116). The stations have almost the same azimuth (328°–329°) from the event. The data are aligned on the *S*-wave times predicted by ISAP91 model.

complicate the record section, namely, the deeper structure near 58°, the red-zone near 60° and the upper slab near 62°. The low-velocity zone (LVZ) is needed to increase the traveltimes and focus the energy near 61°, which produces the large amplitude. Extending the LVZ to deeper depths fits as well but not resolved with only teleseismic data. Note that the mixture of many fast and slow zones scattered throughout the upper mantle makes it difficult to use traveltime alone to resolve details which is probably why the various tomographic models differ, that is, Fig. 3. Adding data at triplication distances greatly helps fix the depths of penetration as discussed in

Table 1. Earthquake used in this study.

Date	Latitude (°)	Longitude (°)	Depth (km)
2007 May 30	52.01	157.78	123
2007 November 16	–2.50	–78.00	114
2008 May 29	63.92	–21.17	12
2008 August 04	49.77	156.70	90
2008 September 03	–26.85	–63.30	571
2009 November 14	–23.01	–66.83	222

Chu *et al.* (2008). However, the complexity of teleseismic waveforms and amplitude helps establish the sharpness of features since the multipath requires strong lateral variation and dipping structure.

In short, USArray is providing the first opportunity to observe the seismic waveform field with enough detail to observe clear diffraction patterns, as presented in this report. Since diffractions are associated with sharp features, they require special source–receiver geometry where the waveform distortions prove highly path-dependent. Not only are the direct arrivals complex along these particular paths, other phases are likewise distorted, Fig. 4, but not necessarily at the same range. Thus, pattern recognition methods can be used to infer structural features as presented in Sun *et al.* (2010) for imaging deep mantle structure.

2.2 Multipath detection

In this section, we introduce the method of analysis that exploits waveform complexity to resolve sharp structural features. Note that the splitting is controlled by traveltime differentials between arrivals, which can be captured by 2-D arrays. A complete decomposition of the wavefield is possible as discussed by Sun *et al.* (2009), a MPD.

To approximate 3-D effects by combining 2-D synthetics with Green's functions G_R^2 and G_L^2 computed to the right and left of the geometric great circle, we can generate the displacement wavefield as a sum of operators:

$$V(r,z,t) = O_L * G_R^2(\Delta_l) + O_D * G_R^2(\Delta_d) + O_L * G_L^2(\Delta_l) + O_D * G_L^2(\Delta_d), \quad (1)$$

where Δ_l, and Δ_d are the radii of the lit and diffraction zone, respectively. $O_{L,D}$'s are the operators weighted by their distances away from the geometric arrival time with the extra time taken to travel to the Fresnel edge (Helmberger & Ni 2005). The 2-D synthetics can be generated analytically (WKM) as in Sun *et al.* (2009) or numerically (FD) as in Song & Helmberger (2007a).

In Fig. 6, we display such a simulation using the lower transition zone structure given in Fig. 5. The upper cartoon displays the 3-D geometry idealized as a box, supposing a simulation at a 45° angle

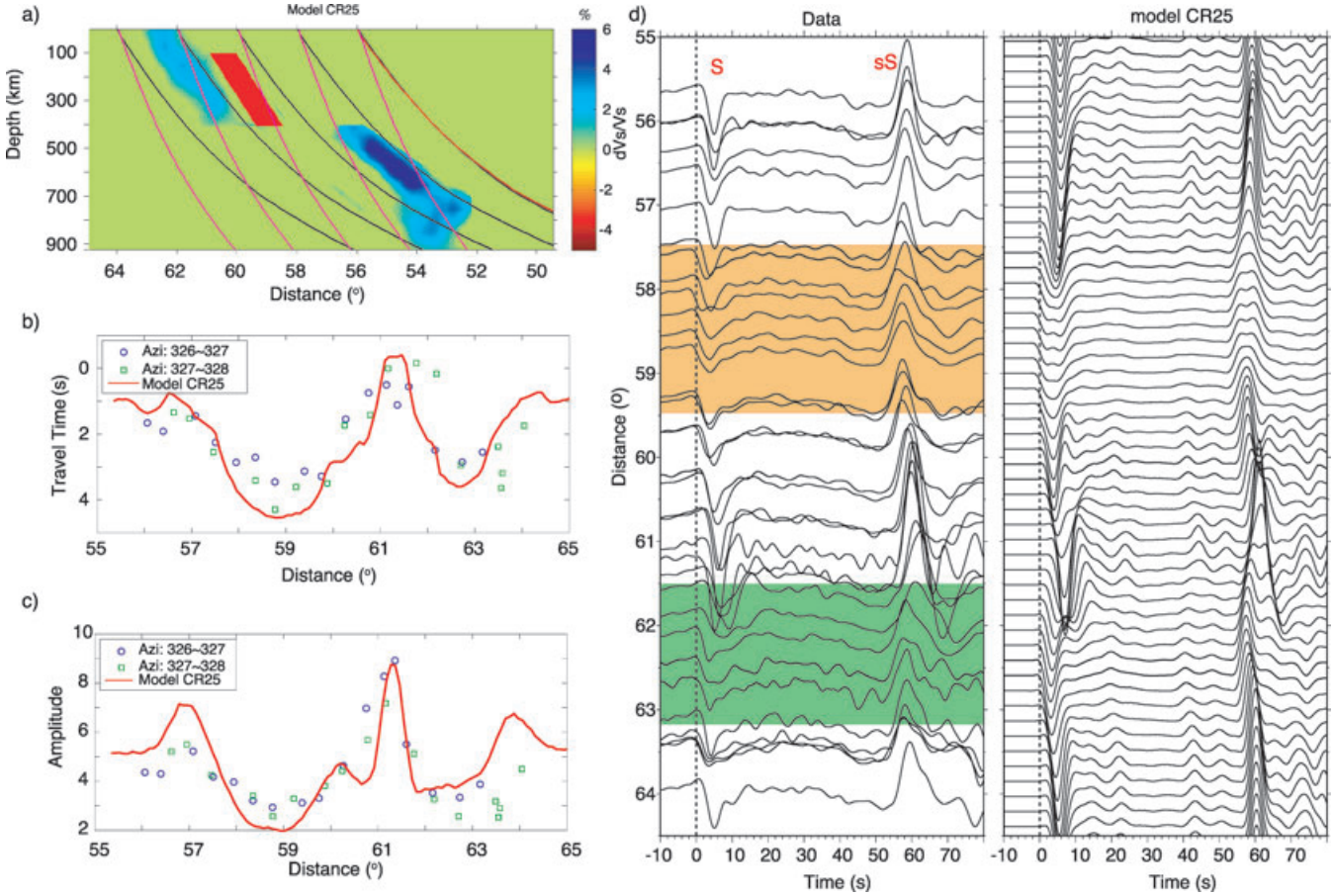

Figure 5. 2-D modelling of the S and sS waveform data from Fig. 4. The best fitting model CR25 in (a) was produced by removing small structures and inflating features producing the multipathing in the P tomographic model from Xue & Allen (2010). The top blue region is inflated by 2.5 and the bottom one is inflated by 4. The comparisons of Traveltime and Amplitude of S are displayed in (b) and (c). (d) Comparison of data against 2-D Finite Difference (FD) synthetics from model CR25. The model produces the strong multipathing around 58° (yellow region) and 62° (green region) for both S and sS phases in the data. The large amplitude at 61° is also predicted by this model.

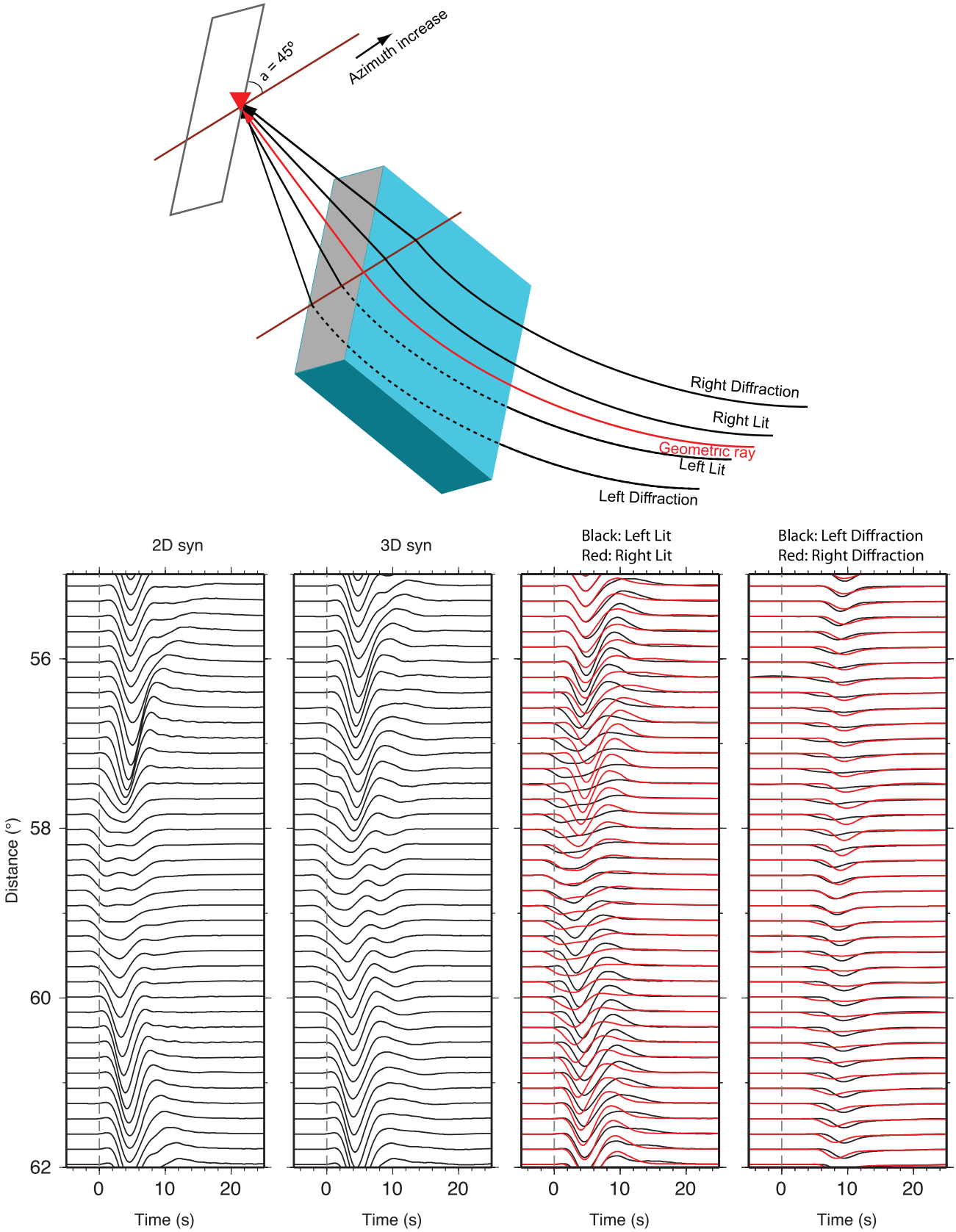

Figure 6. 2-D and 3-D simulation for a slab-like structure in the lower transition zone as in Fig. 5. The ray path has a 45° angle to the strike of the slab. The upper diagram displays the four ray paths sampling the structure, with the red path indicating the geometric ray. The cartoon is appropriate for the red-ray just reaching the slab or near about 57.5°, with the dotted paths (left) sampling inside the slab while the black rays are still outside. The 3-D synthetics are the summations of the 'lit' and 'diffracted' contributions in the right two columns.

between slab strike direction and ray path. Such a geometry will smear the multipathing as demonstrated in the lower columns. The diagram indicates the geometry along with the four sampling paths shifted relative to the geometric arrival by $X_l = \sqrt{\alpha h T/2}$ and $X_d = (\sqrt{2}+1)X_l$, where h is the reference depth (400 km), α the average velocity and T the source time duration.

If the geometric ray path is at right angle to the structure, the 2-D synthetics apply. However, when encountering the structure at an angle, azimuthal paths contribute. Note that the lit contributions are similar but simply shifted in time. We may not observe all these arrivals, that is, the 2-D synthetics sample one-edge than the other where the fast arrival does not become a single pulse. In general, the multipathing can be a combination of both in-plane and out-of-plane (Sun *et al.* 2009) and can be separated for large structures, that is, wavelengths are small compared to size of the structure. If we neglect the longer period diffraction effects, we can greatly simplify the procedure and treat only the left and right aspects of the field.

$$V(t) = O * G_R^2(\Delta_l) + O * G_L^2(\Delta_l) \tag{2}$$

Furthermore, we can approximate the solution with two pulses and assume the pulse has the same shape and different strengths (Sun *et al.* 2009),

$$V(t) = [S(t) + C \times S(t - \Delta_{LR})]/2. \tag{3}$$

$S(t)$ is Green's function from a reference model convolved with an empirical source function, which is the simplest waveform in the array, as found from a cross-correlation search. Δ_{LR} is defined as the time separation, which refers to the lag of the right half of the Fresnel zone relative to the left, or split time. To determine C and Δ_{LR}, we first generate a WKM synthetic (Ni *et al.* 2003) for a reference model to obtain *S(t)*. Next, a simulated annealing algorithm is used to evaluate eq. (3) to obtain the best cross correlation between the simulated waveform and data (Fig. 7) in searching for the best Δ_{LR} and C. We then cross correlate the simulation with the data to measure the timing onset relative to a reference model to obtain Δ_T. An example application is displayed in Figs 8(a) and (c) for the 2-D section discussed in Fig. 4. We included reference lines indicating the 1-D reference model (IASP91) traveltimes. The simplified characterization of the observed pulses captures much of the complexity but does not always have the right shape or arrival time. These features are expected because we have neglected the longer period diffractions (Helmberger & Ni 2005). However, the characterization of the data is improved over cross correlation of the average shape commonly used in tomography. The main improvement is in a method of detecting complexity and its relationship to traveltimes. In particular, when the arrivals become earlier, as at 58° and 62°, they also multipath and drop in amplitude. The amplitude information of the data as a function of frequency is important in mapping velocity heterogeneities as demonstrated in Tian *et al.* (2009). Although there are many ways to parameterize amplitude, we examine two approaches. First, the amplitude can be described as the peak ratio:

$$\text{Amp} = \text{Amplitude}\,(D(t))/\text{Amplitude}\,(S(t)), \tag{4}$$

where $D(t)$ is waveform record for the data relative to the reference synthetic *S(t)*, with this definition and Amp is an independent measurement from the MPD process. If MPD process is considered, we can define the amplitude as:

$$\text{Amp} = \text{Amplitude}\,(D(t))/\text{Amplitude}\,(V(t)). \tag{5}$$

If the multipathing is the only factor affecting the amplitude,

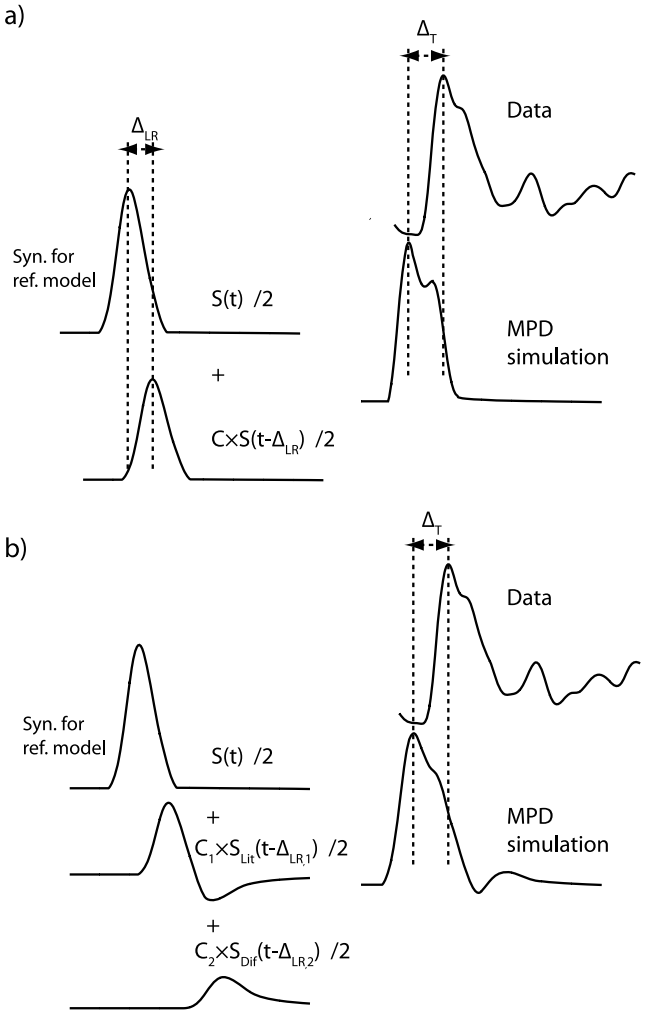

Figure 7. Illustration of the method of MPD. The displacement wavefield can be calculated by adding non-great circle path contributions. If we focus on short periods as in eq. (3), we can only treat the left and right aspects of the field (Sun *et al.* 2009) (a). A given waveform data can be simulated by adding synthetics for a reference model by allowing time shift of Δ_{LR} between them. The two synthetic waveforms are identical. Δ_{LR} is determined by producing the best cross correlation between added waveform and data. Δ_T is time difference between the entire simulation relative to the data or total delay. In (b), the diffraction contribution is included as in eq. (6).

$V(t)$ will have both the waveform shape and the amplitude agreeing with $D(t)$, that is, Amp = 1. For those data affected by focusing or defocusing effect, the Amp can either be smaller or larger than 1. These two amplitude measurements have been included in Fig. 8 with results from eq. (4) given first relative to the values after from eq. (5). Note that the amplitude estimates vary considerably near 58°, where strong defocusing has occurred in the data; in contrast, strong focusing beyond 60° can be detected.

For comparison, if the diffraction parts are included, the eq. (3) can be rewritten,

$$V(t) = [S(t) + C1 \times S_{Lit}(t - \Delta_{LR,1}) + C2 \times S_{Dif}(t - \Delta_{LR,2})]/2. \tag{6}$$

$S_{Lit}(t)$ and $S_{Dif}(t)$ are the lit region and diffracted region contribution, respectively. $\Delta_{LR,1(2)}$ is the time separation between the right half of the Lit (Diffracted) region relative to the left Fresnel zone

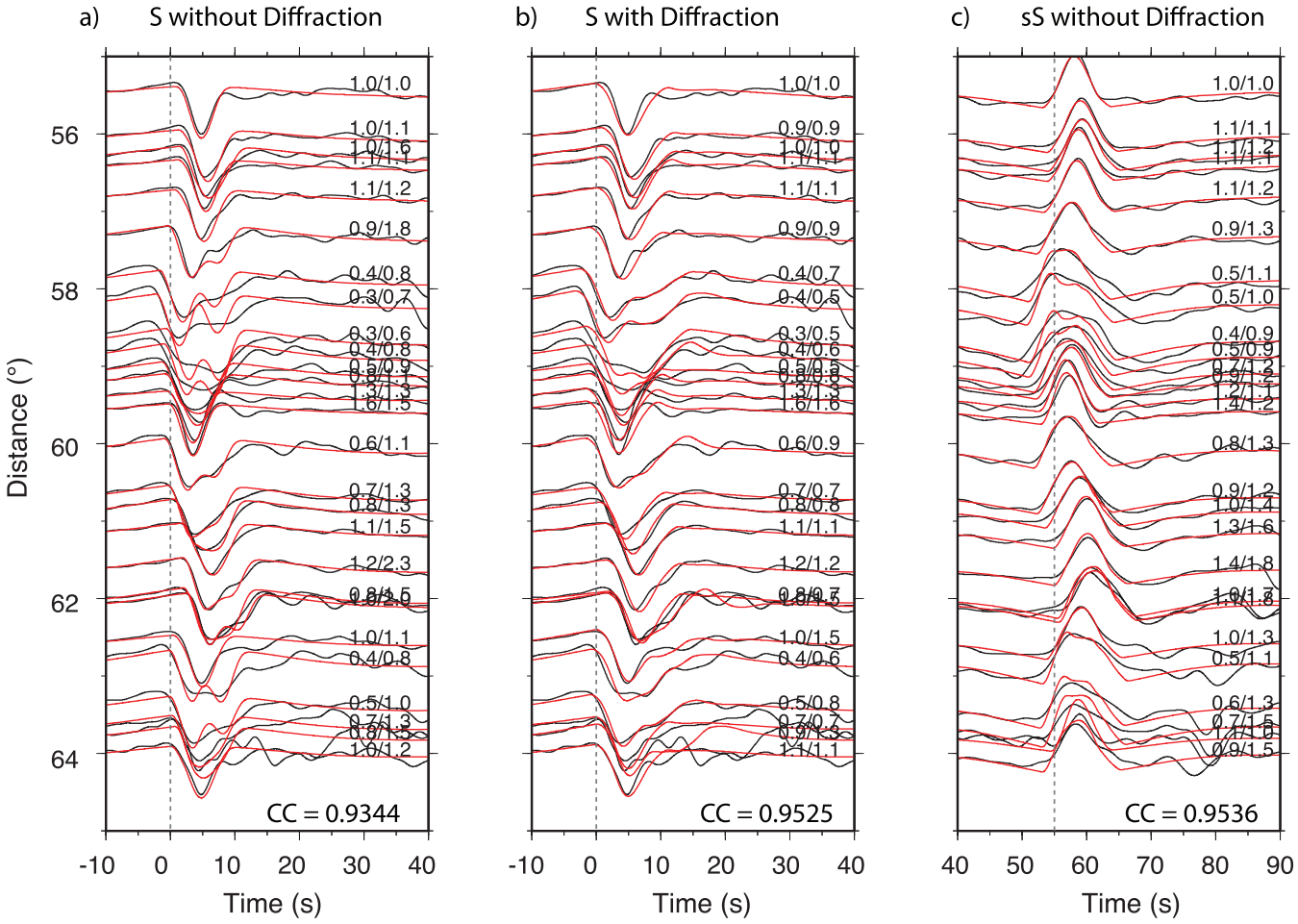

Figure 8. MPD simulations (red) for (a) S and (c) sS waveform observations (black) in Fig. 4. The numbers at the end of each S traces is the amplitude ratio (Amp) defined in eqs 4 and 5, respectively. All the ratios are normalized to the ratios of the top record, which has simple waveform. The MPD simulations with considering diffraction part is displayed in (b).

(Fig. 7b). With the extra-diffracted part, the fit of the waveform is improved (Fig. 8b), especially for the records at 58° with long-period diffraction displayed. The MPD process for sS phase is also given in Fig. 8(c). Because the sS phase follows similar paths near the receiver, they have similar waveform properties.

The Δ_{LR} patterns for S and sS phases are compatible for USArray records for a South American event (20071116) as given in Fig. 9, but the strength of the Δ_{LR} are not the same. Thus, the value of Δ_{LR} in the inversion is strongly depended on the choice of Source Time Function (STF). The longer STF will only generate large Δ_{LR} values for those most distorted waveforms (Fig. 9c). In our study, we typically pick the simplest waveform in the array as STF. Fig. 9(d) gives the Δ_{LR} pattern including the diffraction correction. The result agrees with the pattern without diffraction in (Fig. 9a) in most regions. By introducing the diffraction, the inversion has the ability to fit very small late arrivals, which may not be the real multipathing signal. For the purpose of simplifying the calculation, we will only use the simple form of MPD as in eq. (3) without considering the diffraction.

In Fig. 9(a), strong linear Δ_{LR} anomaly crosses the High Lava Plain (HLP) region. It is at right angles to the ray path, which suggests that we are primarily observing in-plane (2-D) multipathing as modelled in the last section. However, it becomes much more difficult to study 3-D structures because of the added edges and multiple diffractions.

2.3 Pattern recognition

To illustrate azimuthal complexity, we generated 3-D synthetics for relatively simple structures embedded in Preliminary Reference Earth Model (PREM). Although semi-analytical methods can be used as in Fig. 6, we used the 3-D spectral-element method (SEM; Komatitsch & Tromp 2002a,b) for a few structures suggested by the above tomographic models. The first case concerns a plume-like structure idealized as a thin box aligned along an *S*-wave ray path arriving at a vertical position in Fig. 10(a). We then generated a grid of synthetics at the various receivers and produce maps of Δ_T and Δ_{LR}. The edges of the structure produced a few seconds of multipathing forming a small circle with radius of above 2°. For smaller velocity anomalies (–1.5 per cent), the features become less discernable. Thus, idealized plumes are difficult to recognize. Numerical experiments such as this are given in Sun *et al.* (2010). Essentially, for small radii, say 75 km and normal *S*-wave duration (6 s), it becomes difficult to identify Δ_T timing offsets but the slow travelling energy up the pipe still produces broadening of the signal. If the ray path is not aligned with the structure (Fig. 10b),

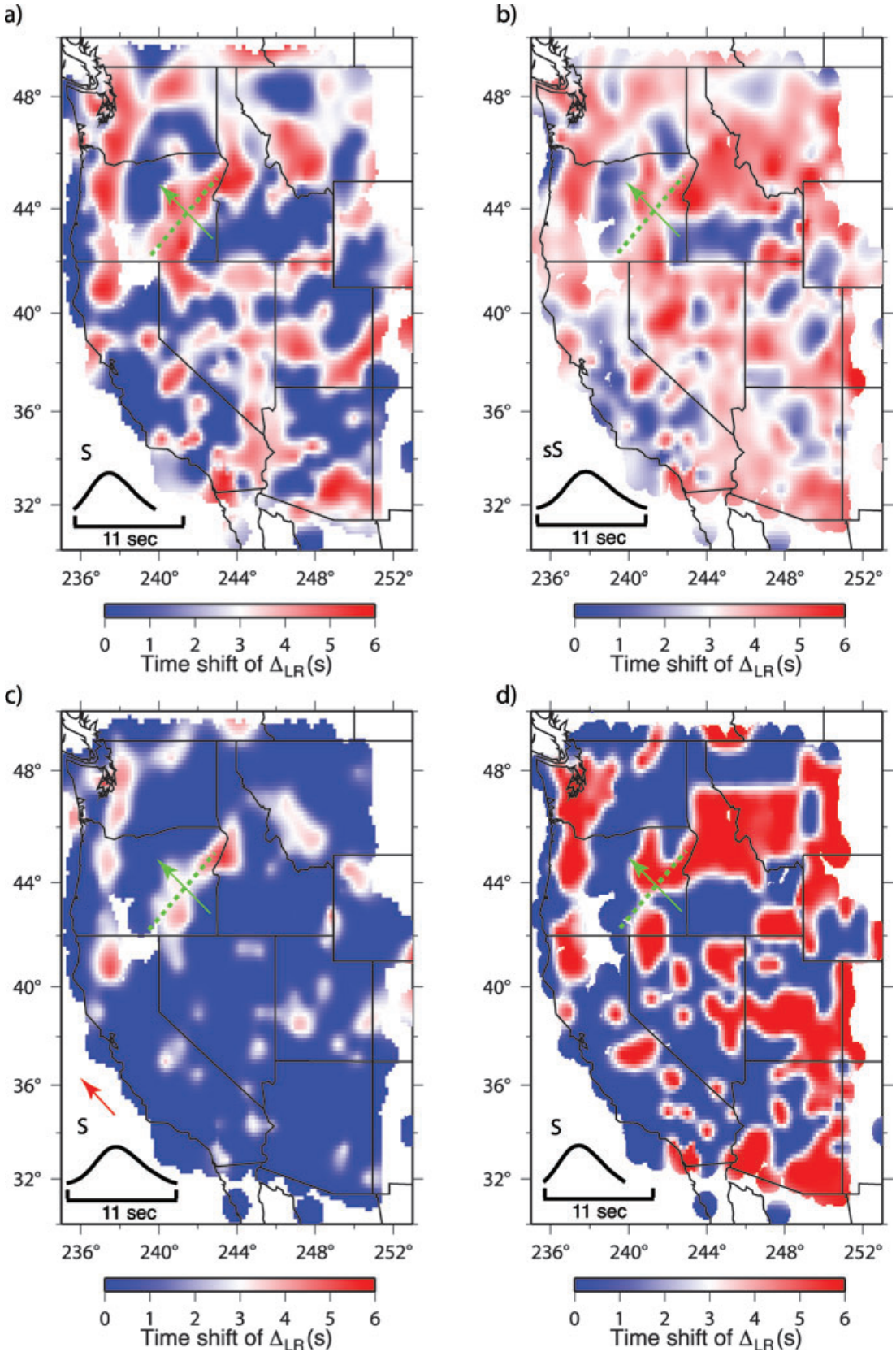

Figure 9. Δ_{LR} patterns for a southern American event recorded by USArray. The Δ_{LR} patterns for (a) S and (b) sS phases are compatible. The patterns depend on the choice of STF. The longer STF will only generate large Δ_{LR} values for those most distorted waveforms (c), that is, the Northern Coastal Region. In (d), the pattern is derived by introducing the diffraction. The arrows in the plot indicate the radial direction from event to USArray. The largest Δ_{LR} values in the eastern Oregon are highlighted with dash line. The line perpendicular with the radial direction suggests that the strong waveform distortions in this region are caused by in-plane multipathing.

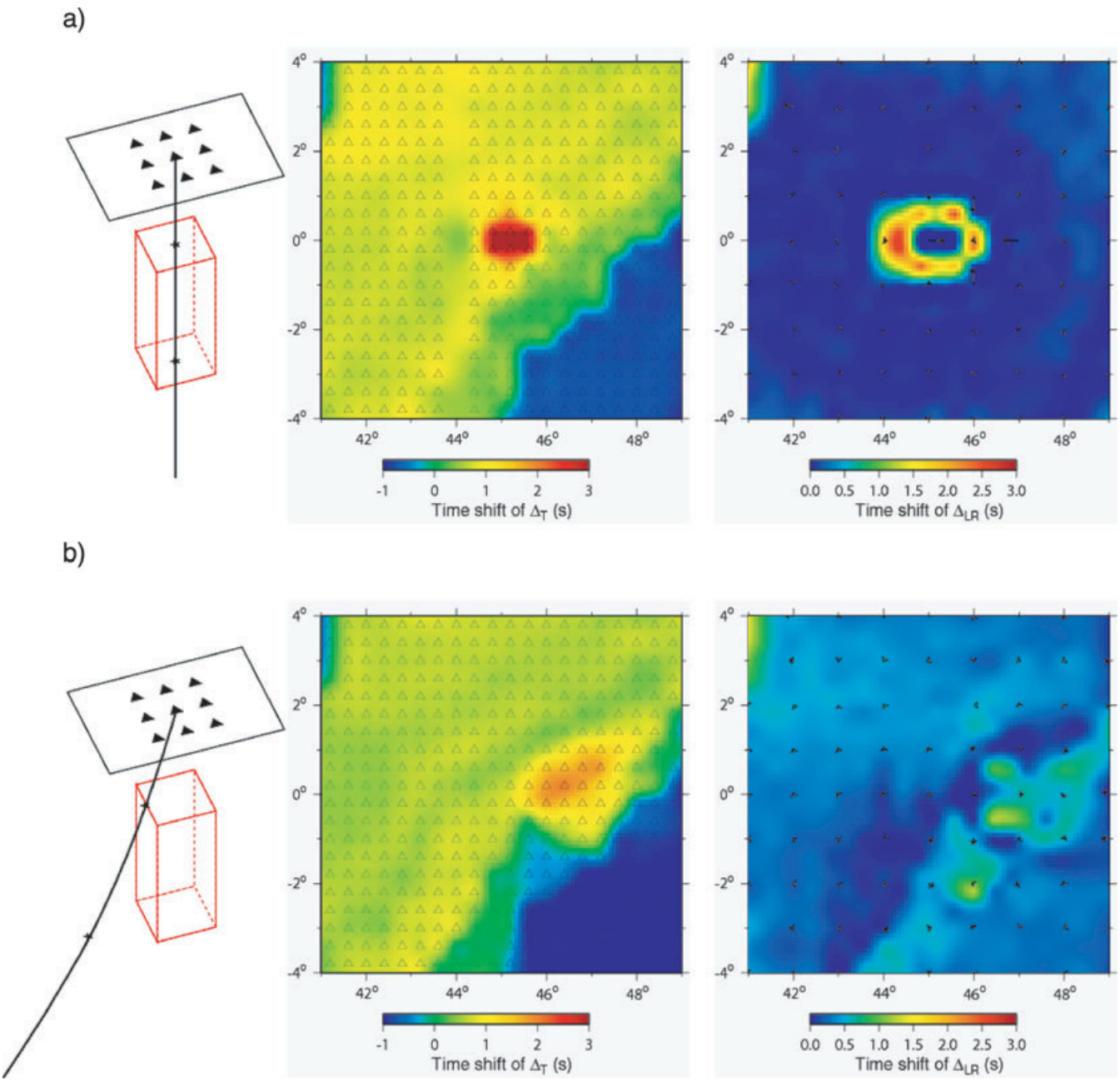

Figure 10. Comparison of the MPD patterns for two different ray geometries. In (a), the reference ray path samples the low velocity structure along the strike. The stations above the structure display the most traveltime delay, but the strong multipathing (large Δ_{LR}) occurs only for stations along the edge. In (b), the ray samples the structure at an angle of 45°, the pattern show less traveltime delay and no obvious multipathing. In both case, SEM 3-D synthetics are calculated and MPD analysis is applied to those synthetics to produce these images, that is, Sun *et al.* (2009).

the images become weak and the identification of the causative structure becomes difficult.

Next, we examine a large-scale structure with dimensions and orientation similar to that proposed for the SRP as displayed in Fig. 1. The model extends from a depth of 100 to 400 km with an 8 per cent *S*-velocity reduction. It has a width of 200 km and is 500 km long. The 3-D synthetics are given in Fig. 11 along with the multipathing parameters. Since the ray paths are arriving along the side edges, they do not display much distortion until paths sample inside the box. Stations with the greatest delays are A11G11 and A11G13 at the southern end, which also have the strongest amplitudes. This is expected for slow paths caused by geometric focusing if there is no attenuation. Azimuthal multipathing is observed along the edges, which are displayed about 1.5° from the most anomalous Δ_T's. In this case, they are nearly the same strengths on each side since the arriving wave front is nearly at right angles to the sides. The Amp pattern is in accord with the Δ_{LR} plot where large Δ_{LR}'s reduce the amplitude. The late arrivals, up to 6 s, are displayed in the Δ_T map. The product of Δ_T and Amp emphasizes the detection of the anomalous slow zone. The product of Δ_T and Δ_{LR} and the product of gradient of Δ_T and Δ_{LR} emphasize the edge effect.

For comparison, we included a second test where the velocity

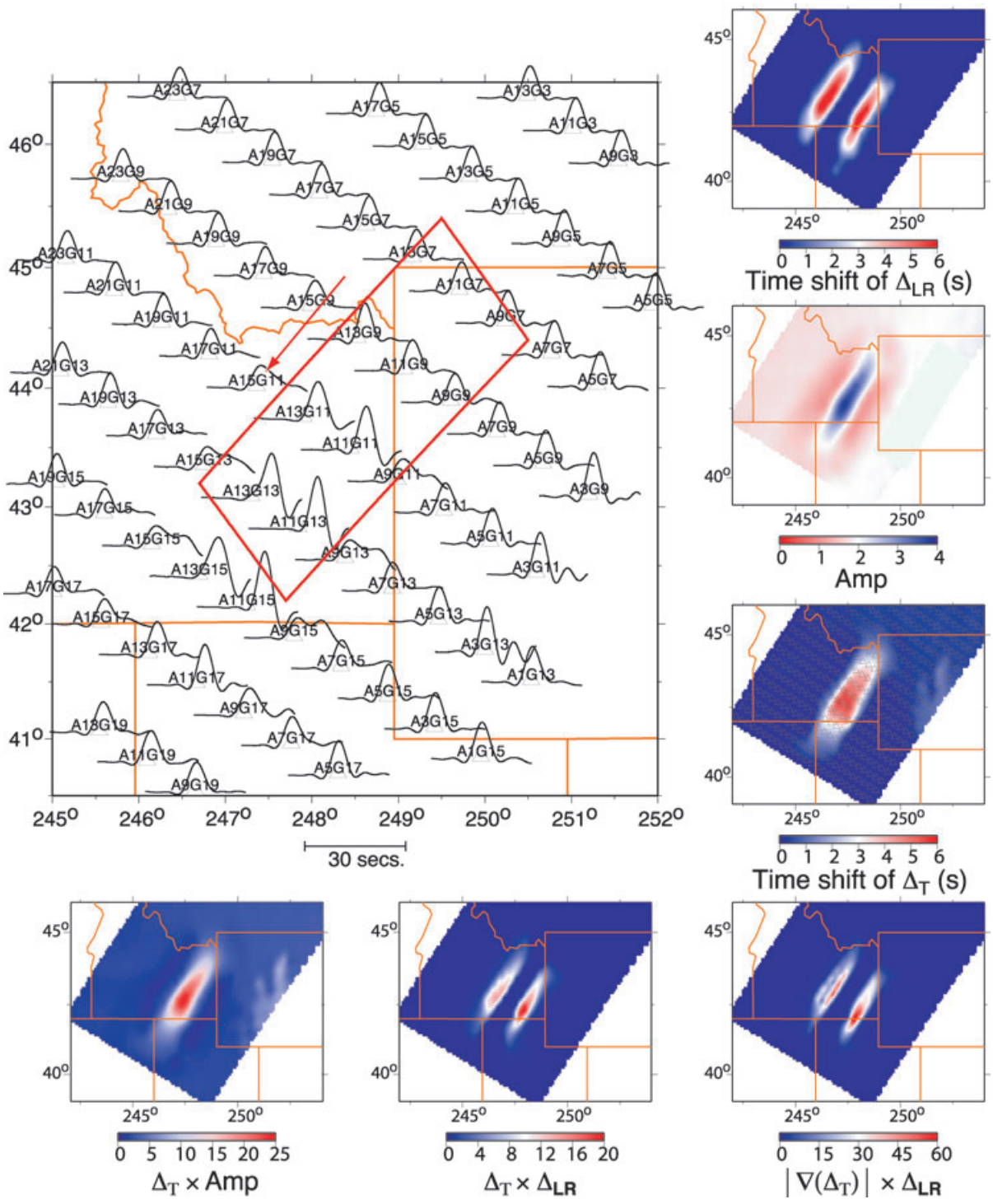

Figure 11. Analysis of 3-D SEM synthetics for a box structure, which extended from 100 to 400 km with –8 per cent shear velocity perturbation. The model is embedded in PREM with a simple source situated for geometry appropriate for an Iceland event recorded at Yellowstone discussed later. Note the increase of S amplitude when sampling the middle of the structure although those waveforms are simple. Multipathing occurs along the two edges, which indicate strong azimuthally multipathing. The bottom row show different combinations of the time shifts obtained from the MPD analysis. ($\Delta_T \times$ amp) pattern emphasizes the low velocity structure. The sharp edges are highlighted by $|\nabla(\Delta_T)| \times \Delta_{LR}$.

anomaly is positive (8 per cent) with results presented in Fig. 12. In this case, the multipathing occurs inside the box and to the south of the box and is not offset much from Δ_T pattern. Note that the amplitude becomes particularly weak above the box and the product of Δ_T and Δ_{LR} changes sign relative to that in Fig. 11. The contrast in pattern can thus be used to help interpret the results from processing real data and in particular, the results for the Yellowstone region discussed later.

In summary, we have generated some simple tools to help recognize patterns produced by fast slab-like structures from slow zones beyond the usual Δ_T measure. We will refer to Dipping Slow Structures (DSS) by computing $\Delta_T \times \Delta_{LR}$ displayed in

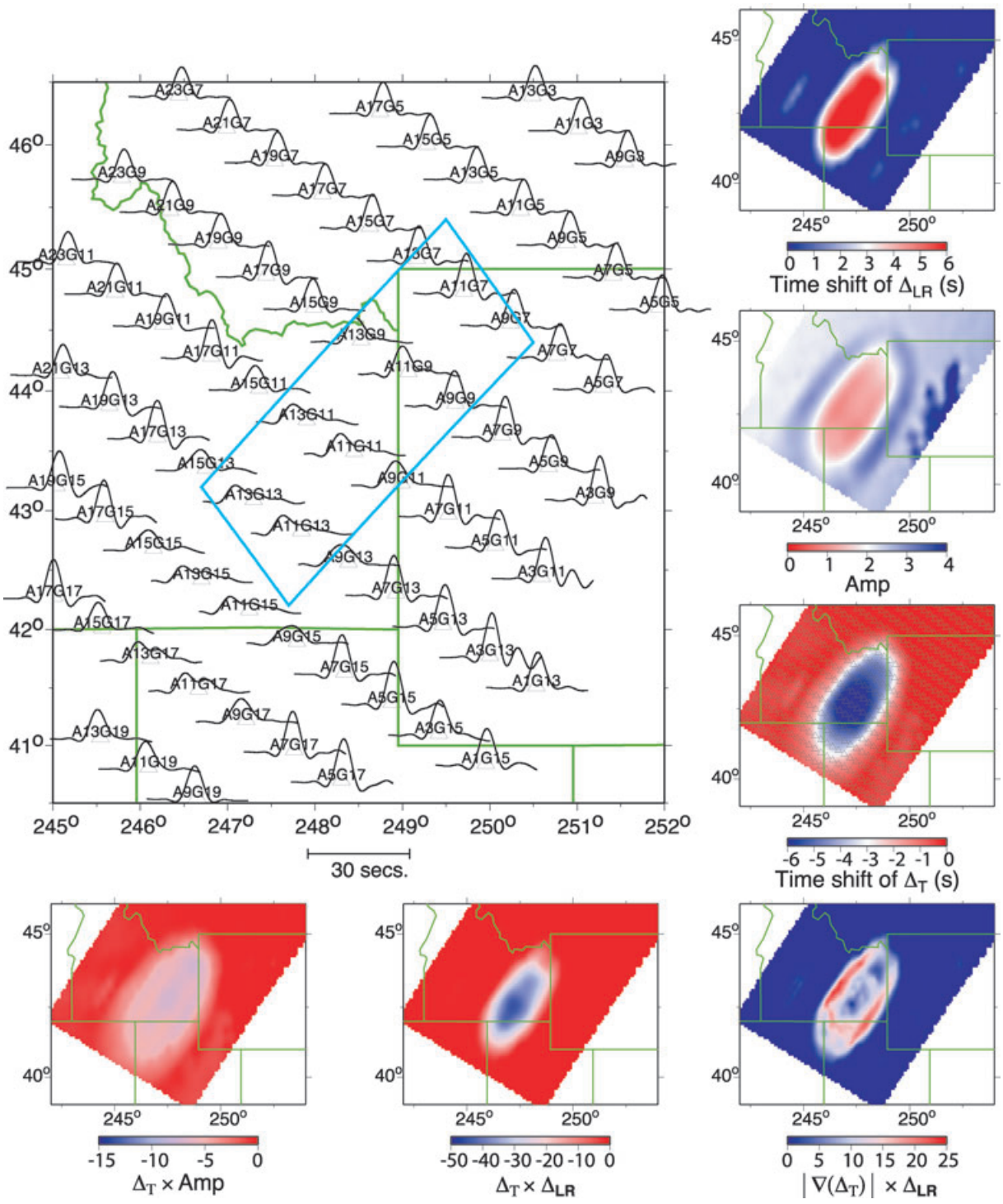

Figure 12. The same geometry as that in Fig. 10 but with +8 per cent shear velocity perturbation inside the box. There are notable amplitude decreases when sampling the middle of the anomaly. The ($\Delta_T \times \Delta_{LR}$) pattern helps define the shape of high velocity structure.

Fig. 11 versus Dipping Fast Structures (DFS) with $\Delta_T \times$Amp in Fig. 12. Another tool to emphasize sharpness is $|\nabla(\Delta_T)| \times \Delta_{LR}$ referred to as an edge detector. We will apply these types of mapping tools in the next few sections on applications to the USArray data.

3 APPLICATIONS TO USARRAY WAVEFORM DATA

Many of the structures beneath the western United States are well imaged by tomography as discussed earlier. Thus, we do not expect to find major new structures here, but we have found some

interesting data sets that will require in-depth modelling to explain such sharp features. Two provinces have been chosen to highlight, namely, the Northern Coastal Region and the Yellowstone Region, although the mapping includes most of the WUS.

3.1 Northern Coastal Region

Earlier in Fig. 5, we displayed a sample of USArray waveform data from an event from the SE along with a 2-D model. Synthetics produced for NW arriving response are simple as discussed in Song & Helmberger (2007a) for a similar geometry. The alignment of ray paths with slab structures as displayed in our 2-D modelling is required for multipathing. Indeed, strong multipathing is evident along the Northern Pacific Coast from the South American event (20071116) starting at the Mendocino triple junction, Fig. 13. The amplitude ratio of the data relative to the reference model (eq. 4) is given in the second column, which correlates well with the MPD mapping. As discussed earlier, the amplitudes vary about a factor 4 or 5 (Fig. 8). Because we want to compare different events, a common scale will be used from 1 to 4 with a few stations at the extremes. The fast Gorda/Juan de Fuca slab is also apparent to about the Oregon–Washington border where some strong focusing occurs providing evidence for the low velocities on top of this slab as discussed by Xue & Allen (2007, 2010). A second band of multipathing occurs at closer distances as again observed in Fig. 4 caused by the deeper anomaly beneath Nevada. Xue & Allen (2010) argue for an older slab structure, perhaps, a piece of Fallon slab. This interpretation of a slab-like feature is supported by our results and the tomographic images from Schmandt & Humphreys (2010a) as is the relatively slow feature sandwiched between the two slabs. These features are enhanced in the fifth column in Fig. 13 with the strong DSS patch beneath the Oregon–Washington border (and up into central Washington) and SRP. The DFS map is displayed in the fourth column. We have included the mapping of $|\nabla(\Delta_T)|\times \Delta_{LR}$ to search for sharp features in the column on the right. Four sharp features occur, two along the Juan de Fuca slab where the seismicity is the highest, one at the northern edge of the Yellowstone Region and one beneath the Tahoe Region.

These structures are less apparent from the NW Kamchatka event event (20070530), lower row, which does not display much complexity involving the Juan de Fuca plate as given in the lower panels. However, there is some interesting structure along the Washington–Idaho border, which appears to be a relict slab (Schmandt & Humphreys 2010a). This feature can also be observed for events with better coverage of the Yellowstone structure discussed next.

3.2 Yellowstone region

There has been a great deal of geophysical work done on the Yellowstone hotspot and its apparent track along the SRP with several special seismic displacements and, indeed, this region produces waveform complexity as can be seen in Fig. 13 although somewhat subdued. We examined events arriving from many azimuths and found NW events producing the strongest multipathing. Here, we chose an event from Iceland and two from the NW to process. The paths from the Iceland event are roughly aligned with the trend of the SRP, which is ideal for testing the nature of edges. A sample of waveforms for this region is presented in Fig. 14 along with their traveltime delays Δ_T. The waveform complexity is obviously stronger to the north and offset from the Δ_T anomaly as in the theoretical pattern discussed earlier in Fig. 11. In fact, both the Δ_T and Δ_{LR} observations are at the same signal strength as that modelled, implying a thickness of 300 km at –8 per cent drop, or 600 km at –4 per cent since only the differential traveltime is estimated with this level of simulation. There is an extension of late arrivals to the north of Yellowstone suggesting another complication that also appears in some recent tomographic images (Tian *et al.* 2009). The results from the MPD analyses is presented in Fig. 15. While the SRP data displays the strongest Δ_T delays, other structures are also outlined such as the Colorado Plateau. Structures to the north show the strongest multipathing where previous events have detected. Note that the DFS blue zones agree very well with those from Fig. 13 when migrated downward. Since this structure can be seen at all azimuths, it must be nearly vertical or perhaps a curtain-like-structure as suggested by Schmandt & Humphreys (2010b). The amplitudes generally track the Δ_{LR} pattern but are somewhat subdued. The DSS pattern is strong for the SRP structure and somewhat more complicated for the RGR zone implying eastward dipping structure along the Rocky Mountain Front. However, the strongest edge features appear to be associated with the northern boundary of the SRP and Yellowstone.

In Fig. 16, we display the results from processing events from the NW for two networks. The upper panel contains data recorded by the Yellowstone Intermountain Seismic Array (Waite *et al.* 2006) where we have included both the broad-band observations along with the MPD simulations. The lower panel contains the results from USArray. Both sets of data show the Δ_T bull's eye on Yellowstone as in the Iceland event. However, the Δ_{LR} pattern is displaced to the NW. These two sets of observations have a mostly circular pattern with dimensions of about 1.5°, similar to that displayed earlier in the SEM simulations (Fig. 10). The ray paths associated with these patterns arrive from the NW where delays up to 15 s have been reported at some stations, that is, LKWY (Fig. 14; Waite *et al.* 2006). Part of this delay can be contributed to the Yellow Caldera (Chu *et al.* 2010), but most of it is coming from the mantle. Waite *et al.* (2006) produced a tomographic image explaining their traveltime observations with a NW dipping structure displayed in Fig. 17(a). The velocity section is from NW to SE, with a record section displayed to the right passing through the anomalous region. Reference lines are added to indicate the late arrivals near 67.6°. On the left are two synthetic record sections generated by 2-D FD code discussed earlier. Note that inflating the Waite's tomography model (OSAVS) by a factor of two does a good job fitting traveltimes. With this inflation, traveltime changes of over 6 s can be produced in agreement with the Iceland data. Moreover, the inflated OSAVS model does a good job of matching data from other azimuths as displayed in Fig. 17(b).

However, this model does not explain the secondary arrivals indicated by the red arrows in (a) and the strong Δ_{LR} estimates given in Fig. 16. The lower panel (c) provides a possible explanation for the extended complexity. The hybrid diagram of velocities is taken from the Fig. 18 from Smith *et al.* (2009), that is used to explain the Yellowstone swell and compatibility with the regional mantle flow pattern. The structure dips towards the NW along the same corridor discussed above. The synthetics on the left (model YS11) contain such a plume-like feature with an extra-leg added along the S-ray path to enhance the secondary arrival (red arrow in panel a). Many of the observations in Fig. 16 show such complications. The patterns are nearly circular indicating the 3-D nature of these small structures similar to the numerical results presented earlier. But we lack the resolution on how deep this plume-like structure extends. Thus plume-like features require dense sampling with special source–receiver geometry for their detection. In short, it appears that deep relatively narrow structures may not influence Δ_T directly

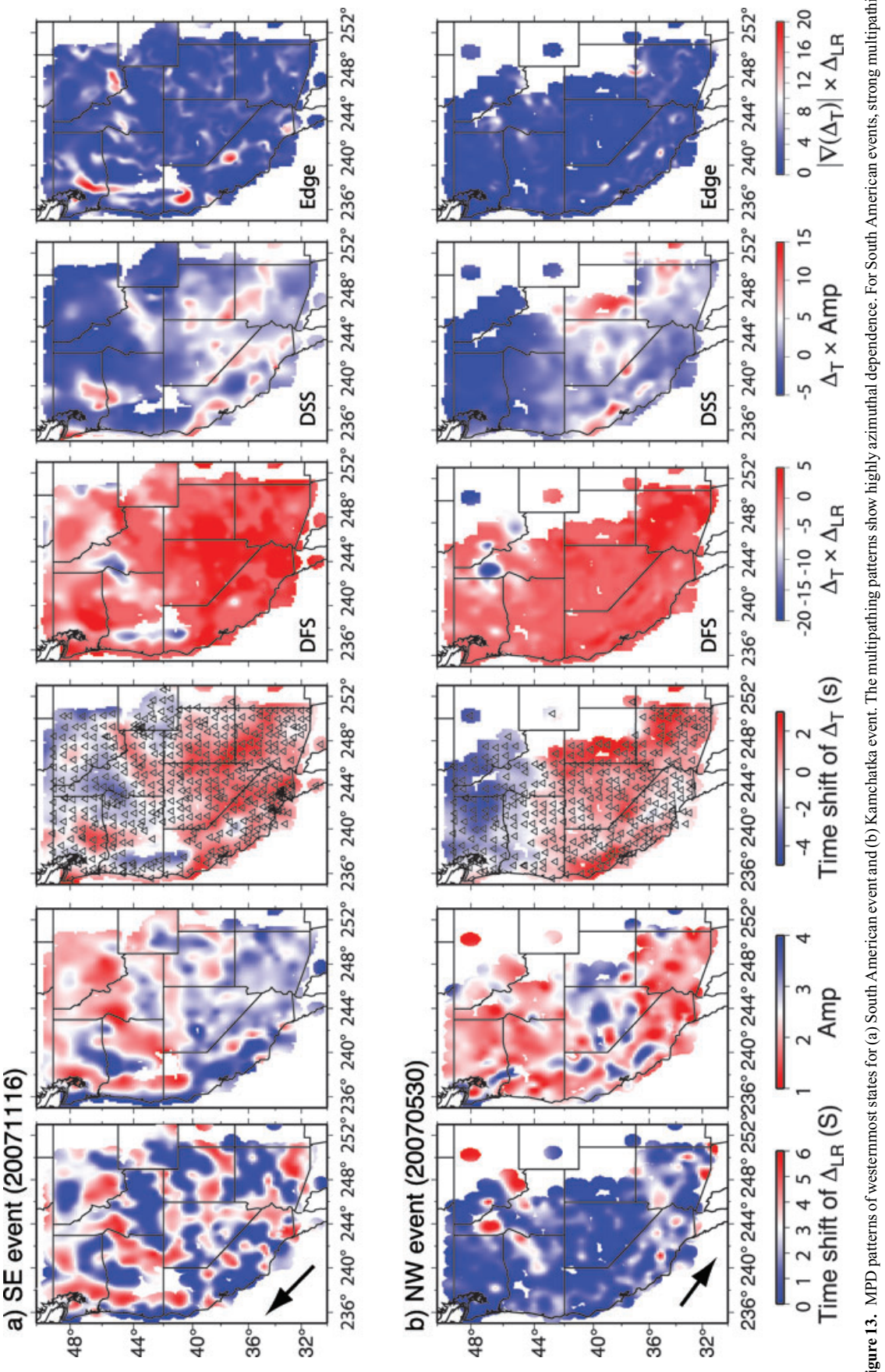

Figure 13. MPD patterns of westernmost states for (a) South American event and (b) Kamchatka event. The multipathing patterns show highly azimuthal dependence. For South American events, strong multipathing occurs along the northwestern coast. But these regions show weak multipathing when the events come from the north. The azimuthal dependence indicates that the multipathing is highly directional. The preferred strong multipathing for the event from the south suggests that the anomalies in the upper-mantle dip to the south, which gives the strongest multipathing when rays paths travel along the structural edges.

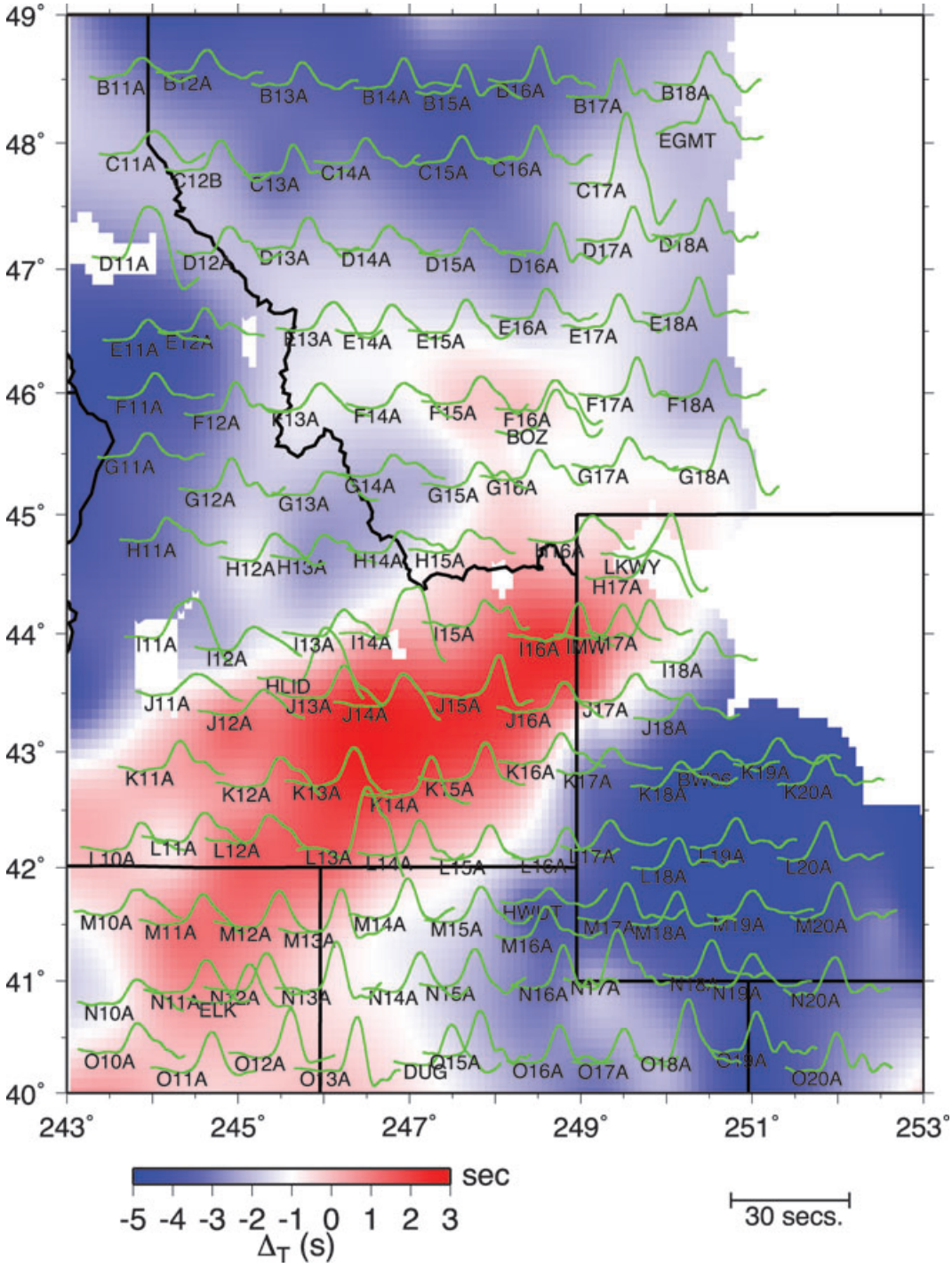

Figure 14. Δ_T pattern together with the *S* waveform records for the Iceland event (20080529). The most delayed data along the SRP have relatively simple waveforms. The strongly distorted waveforms are along the northern edge of SRP.

and can only be detected by modelling secondary arrivals. In this case, the amplitude of the first arrival may not be that dependent on the gradient of Δ_T but involve more of the wavefield including other phases.

4 DISCUSSION

In this study, we used MPD for examining the USArray waveform data. The patterns of strong multipathing provide the locations of sharp features and they can be used to infer penetrating mantle features. Many of the directional properties can be relatively strong as indicated in Fig. 13. Note that while the event from the SE produces numerous structures ranging up to 6 s, the NW event displays subdued responses along the coast. As displayed in the simulations, this corresponds to above a 4 per cent jump in velocity along a 400 km strip if the ray path is aligned. Generally, the amplitudes are anticorrelated to Δ_{LR} as expected, but can be also affected by focusing and attenuation. Obviously, attenuation can have an effect

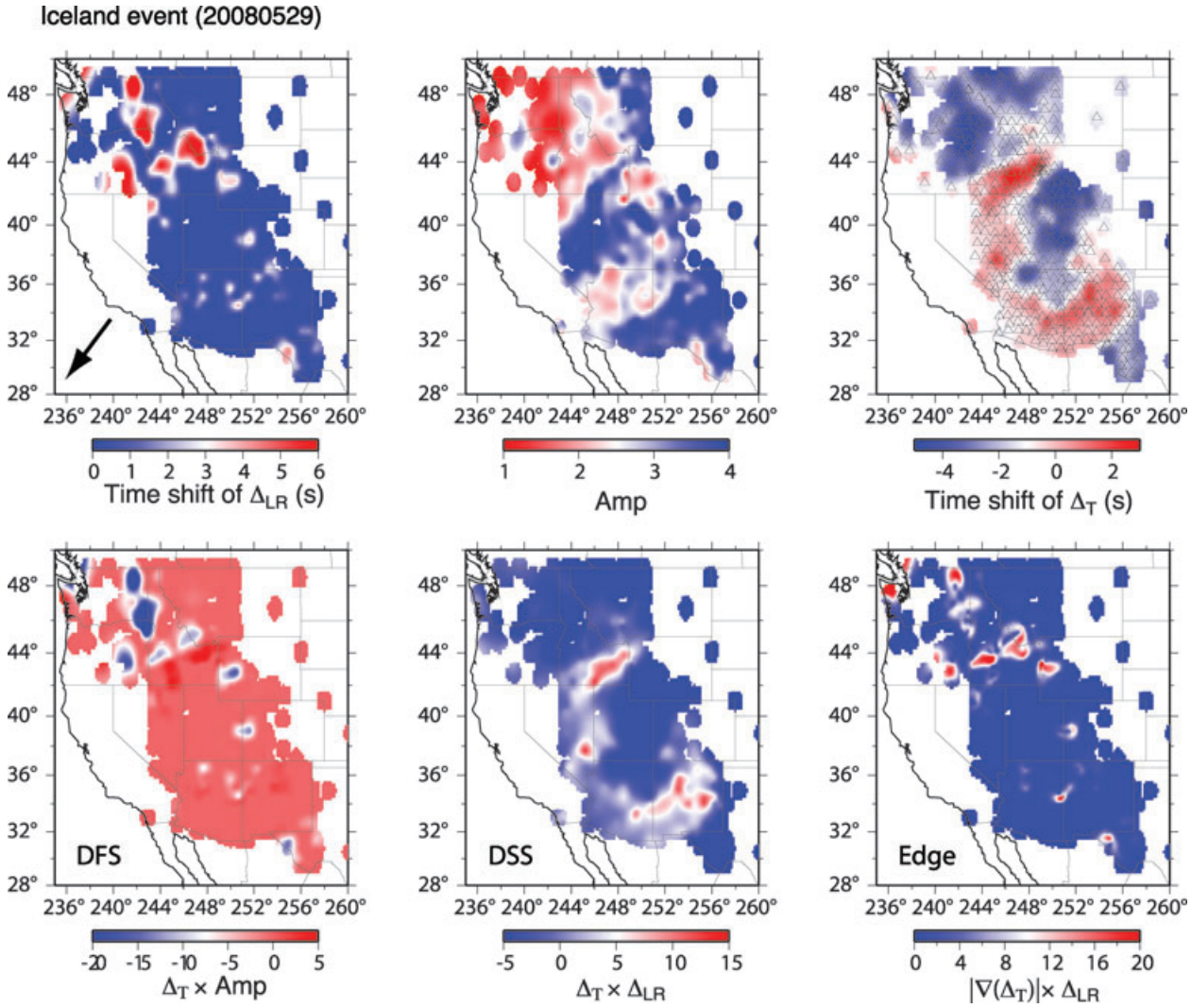

Figure 15. MPD patterns for the Iceland event in Fig. 14. The pattern clearly displays strong multipathing at the northwestern edge of Snake River Plain and northern Idaho.

on altering the amplitude. However, several regions with low amplitude are fast anomalies, which disagrees with conventional wisdom. For example, in Fig. 5, we presented a 2-D model that matches many of the properties of a corridor of observations sampling both the deep structure and shallow structure beneath Nevada and Oregon.

We have attempted to enhance DSS zones by plotting the product of Amp with positive Δ_T (late arrivals). Several anomalies appear outlining the well-known plume-like structure beneath the Washington–Oregon border dipping to the south and a structure dipping to the northeast beneath southern Utah (St. George). The product of Δ_{LR} and Δ_T (early arrivals) highlights fast structures with strong features beneath the Washington–Idaho border, discussed by Schmandt & Humphreys (2010a).

The sharpest features are displayed in Fig. 13 with the southern end of the Gorda-Plate and the slab-flexure near Seattle enhanced. Both features have deep seismicity. Another dipping structure appears beneath Lake Tahoe which also has deep seismicity, Smith *et al.* (2004). This feature can be identified from NW events, which suggests a strong vertical structure or a slow curtain-like feature. If we average the two images, the sharp edges are reduced in strength but are still detectable.

In Fig. 18, we averaged the five events analysed in this report. As listed in Table 1, we chose two events from the SE and NW and the northeast event from Iceland. The two NW events produced strong multipathing of the Yellowstone structure while the SE arriving events highlights the slabs. We migrated these maps downward to 200 km for a reference level although we cannot expect the anomalies to behave as point sources. However, they do identify many of the features seen in some tomographic models.

The Δ_T map Fig. 18(a) reaches over 8 s with all of the BR province and California appearing slow. Many of the early upper-mantle models based on well-known traveltimes from nuclear explosions and waveform modelling mapped out these features. Thus, the existence of a strong low-velocity-zone beneath the pink zone (BR) at depths between 65 and 165 km can explain the North–South basis (Burdick & Helmberger 1978; Grand & Helmberger 1984). However, surprisingly this region is relatively free of sharp features and corresponds to an interesting history of North–South magmatism evolution (Humphreys & Eugene 1995).

There are a few features around the edges of the Colorado Plateau with the strongest denoted in Fig. 18(d) with zone 1. These features are probably associated with magmatism as discussed by Roy *et al.* (2009). A double feature is denoted in zone 2, which

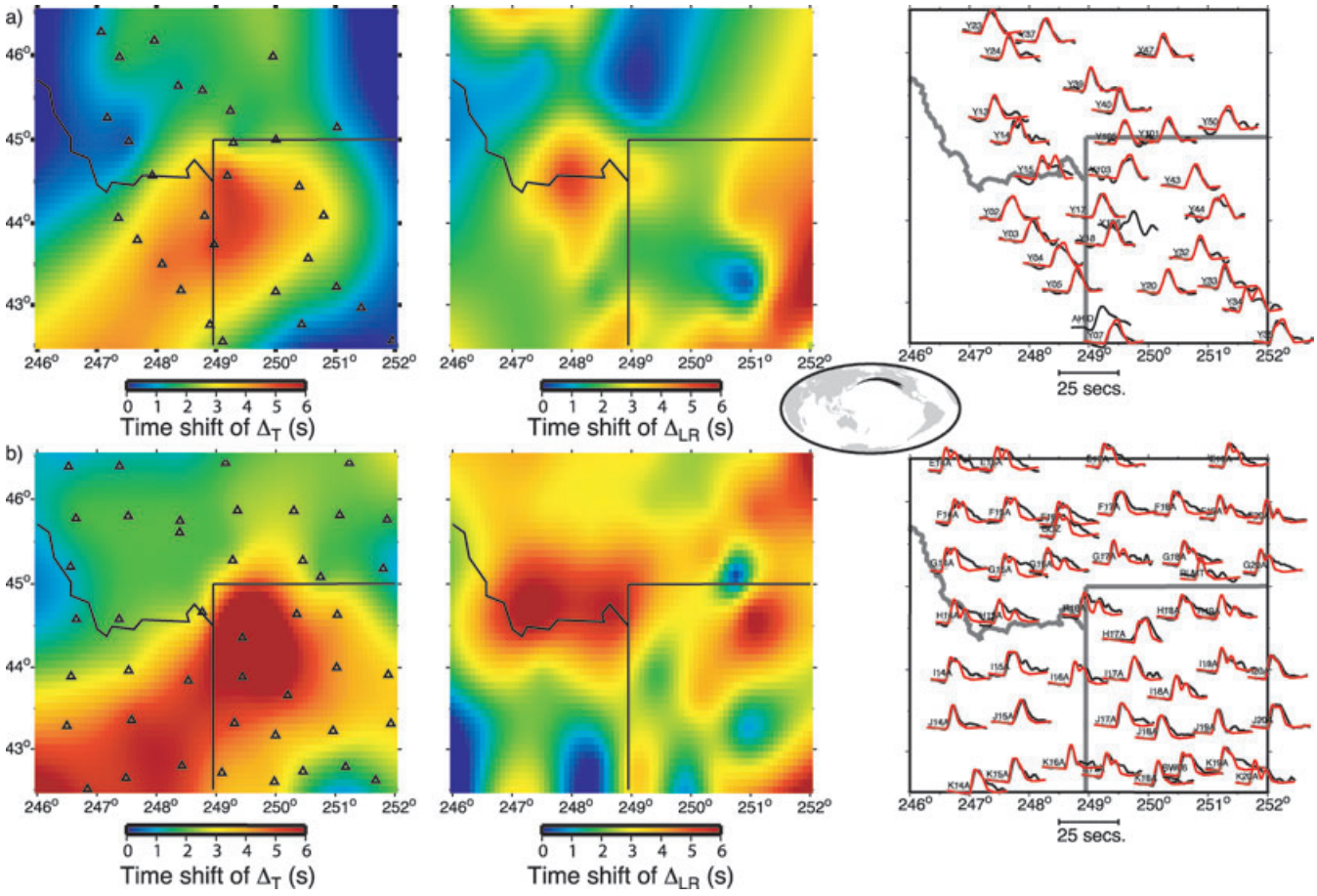

Figure 16. MPD patterns of direct S for Japan events recorded by (a) Yellowstone Intermountain seismic array and (b) USArray. Both patterns show large traveltime delays beneath SRP. The records for stations just above the Yellowstone caldera (H17A) shows very late arrivals, which indicate possible magma-related shallow low velocity structure. Both Δ_{LR} patterns have large values at the north of SRP, which indicate strong multipathing.

is caused by the two SE events having a slightly different geometry, but probably sampling the same dipping-slab edge. Most of the sharp features occur beneath geological boundaries with the extended Cascade Range (CR) containing a string of anomalies from the Gulf of Mexico to Canada. These features appear to be chunks of slab dipping in several directions along with neighbouring DSS zones. Their dimensions are similar to the simulations given in Fig. 10 and probably have deep DFS roots. Some of these could have neighbouring slow-plume-like zones as discussed by Xue & Allen (2010). The primary reason for choosing the XA model for waveform testing was searching for a model with dipping structure as exploited in the Song & Helmberger's (2007a,b,c) papers. Most of the tomographic images for WUS are dominated by rather flat lying structures in contrast to the XA models, as can be observed in comparing some of these structures in Fig. 3. The geometry of slabs such as the one beneath Nevada encountering the 660 km transition is one of the key issues addressed in global circulation modelling. That is, does it flatten-out on top of the boundary as in the Tian model or does it penetrate into the lower mantle as in the XA model, as suggested in recent mineral physics analysis (Ganguly *et al.* 2009). This issue will be further pursued in future efforts.

In summary, these model display great complexity which does not look plate-like in contrast to the Pacific Basin that does (Tan & Helmberger 2007). In short, plate tectonics on continents appears to be heavily influenced by geological history. The downside of this is the great complexity required in modelling. The upside is that it could provide the evidence for understanding past plate tectonics. How far inbroad does this complexity persist? In this case, it appears to be continuing eastern as USArray marches forward as displayed in Fig. 19 where we have the first sample of regions with no previous stations, that is, Nebraska and the Dakota's.

As in earlier figures, we include the waveform observations along with the multipathing processing. The traveltime anomalies are just as intense as those presented earlier. Both the Δ_{LR} and Amp anomalies are strong and in excellent agreement and apparently associated with the Black Hills structure. One simple interpretation of such features is in terms of vertical tectonics. The basic concept is that the cratons are depleted in iron and float about without substantial disturbances (Jordan 1978). However, lithospheric instability manifested by delamination or detachment can occur when encountering a hot upper mantle (King & Ritsema 2000; Song & Helmberger 2007c). The key for this to happen is the R measure or $\mathrm{d}\ln V_s/\mathrm{d}\ln V_p$. If R is low, near one, sinking detachments are predicted. In contrast, subducted slabs have relatively high R's and are naturally heavy and cold and probably sink to great depths. We have not addressed the *P*-waves here, but becomes the fundamental issue in interpreting the many complexities in the various models and how to interpret the deep anomalies detected here and in the tomographic models. What happens to sinking craton detachments when they warm-up?

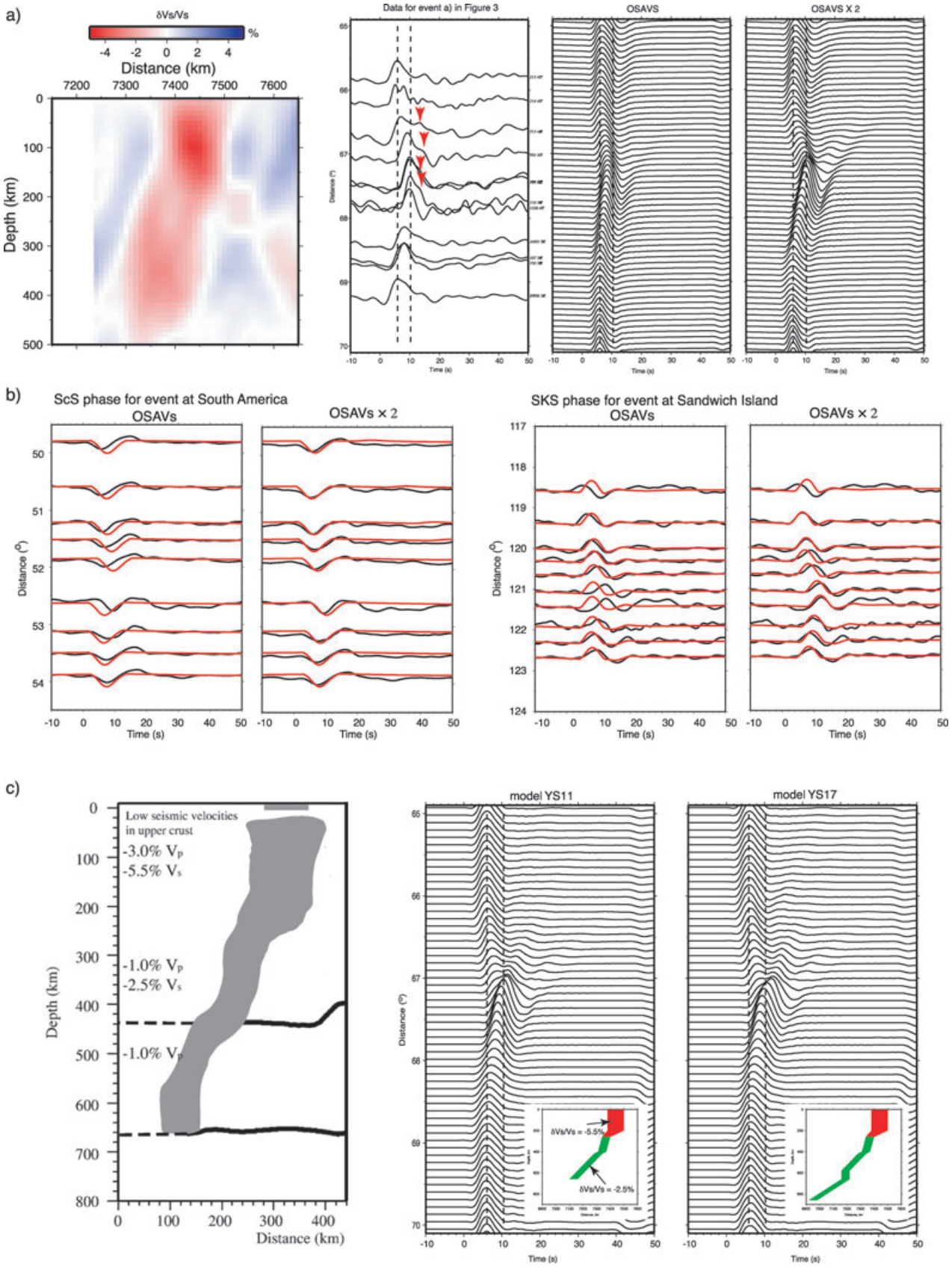

Figure 17. (a) Shear velcoity tomographic model OSAVS (Waite *et al.* 2006) beneath Yellowstone together with the predicted synthetics. By inflating OSAVS model by a factor of 2, the synthetics fit the traveltime very well but lack of waveform complexity in the records from a Kuril island event. (b) Both ScS and SKS (black) for events from South show simple waveform and can be well fitted by inflating OSAVS model by a factor of 2. The hybrid models (YS11 and YS17), with the same structures above 410 km as Smith *et al.*'s model (left diagram), predict second arrivals.

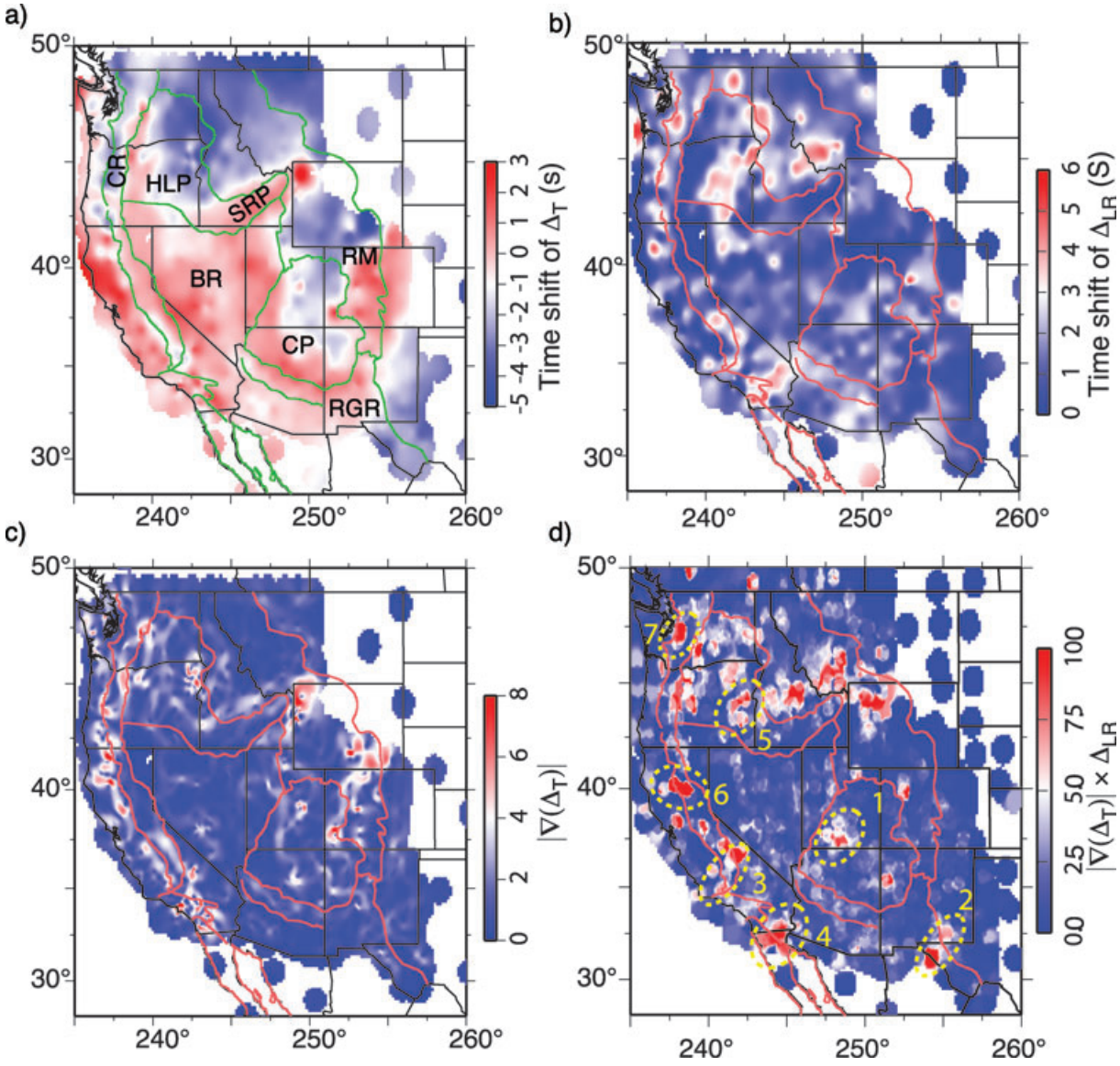

Figure 18. The averaged pattern for five events. All the patterns are migrated to 200 km along the ray paths. The principal geological features are marked, including the Cascade Range (CR), the High Lava Plain (HLP), the Snake River Plain (SRP), the Basin and Range (BR), the Rock Mountain (RM), the Colorado Plateau (CP) and the Rio Grande Rift (RGR). The $|\nabla(\Delta_T)| \times \Delta_{LR}$ map in (d) outlines many small-scale sharp features beneath WUS, such as (1) Colorado Plateau, (2) western Great Plains, (3) southern Great Valley, (4) Salton Trough. Many of these features are interpreted as lithospheric instabillties in Schmandt & Humphreys (2010a). Other sharp edges, that is, (5) eastern Oregon, Juan-de Fuca subduction at (6) Mendocino and (7) Seattle are displayed in the map as well.

Obviously, they stall and return to the surface, perhaps, looking like reversed subduction. Detailed modelling can address these rather fundamental issues.

5 SUMMARY

With the advent of USArray, there is an unprecedented opportunity for investigating the seismic structure in a region that has and is undergoing numerous tectonic changes. As demonstrated in this report, this data set displays waveform complexity related to these structures from events at all ranges and localizing the sharp edges causing these features is difficult. To accelerate this effort, we have developed a new method of processing array data that addresses sharpness directly by detecting diffraction patterns called a MPD. In its simplest form, we suppose that body waveforms can be expressed by two arrivals, a left and right splitting of the Fresnal zone (Δ_{LR}), a composite lagged time (Δ_T) and scaled in amplitude relative to a reference model. Typically, the mapping of Δ_{LR} proves highly directional and driven by geometry as in optical experiments. We applied this methodology to a number of 3-D synthetics (SH) in a training exercise and also derived products of these measures involving$\nabla(\Delta_T)$, Amp and Δ_{LR} to aid in recognizing sharp features. Next, we processed USArray data and found results with similar patterns.

Our results indicate that WUS has a large number of small-scale dipping features mostly tilting towards the SE, similar to the model developed by (Schmandt & Humphrey 2010a). These features have many different scale lengths, 50 to 200 km and Δ_{LR}'s ranging from 3 to 6 s. A slab edge 600 km long with a 4 per cent shear velocity jump

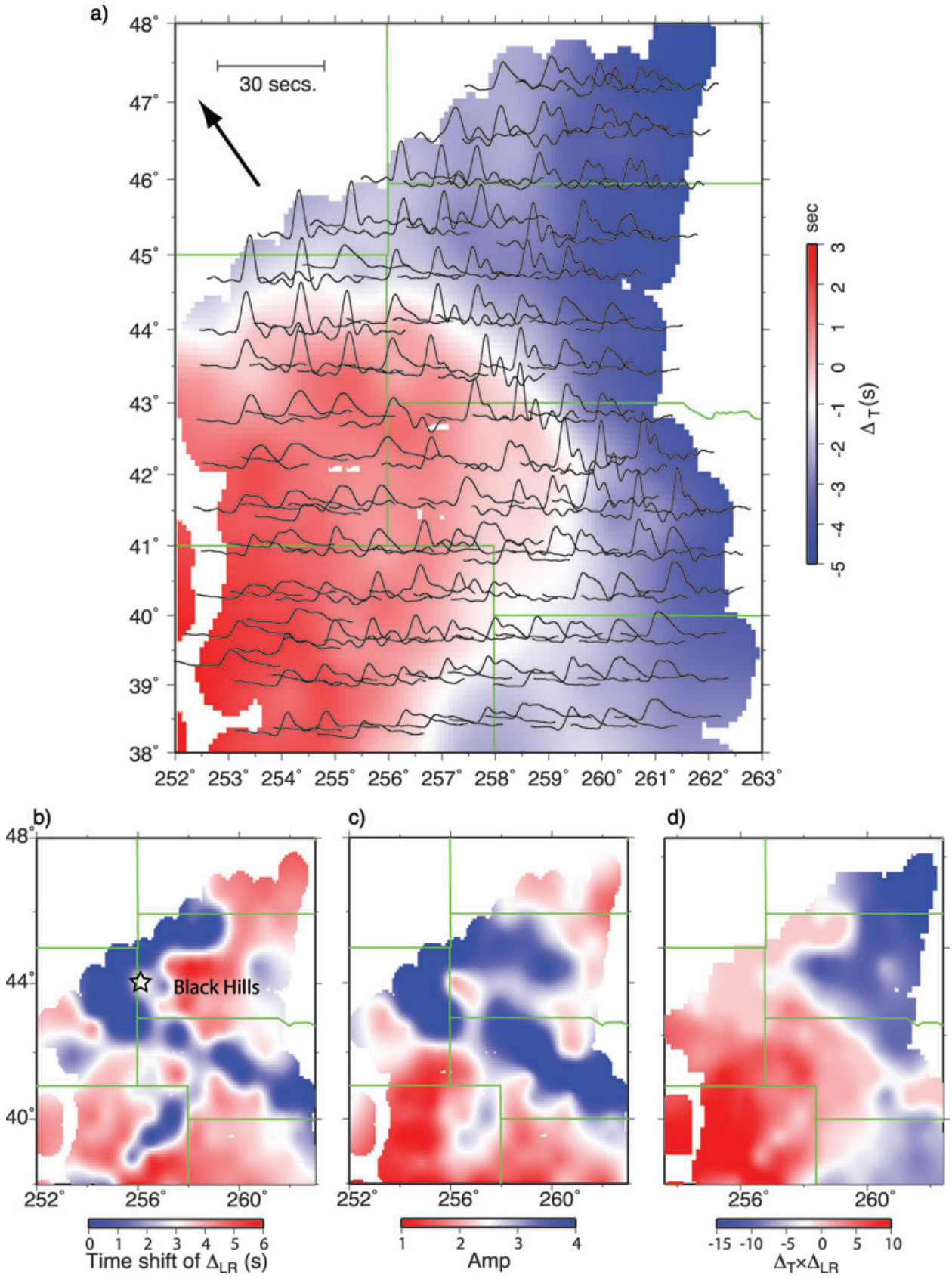

Figure 19. MPD patterns for USArray stations covering the Great Plains region from a South American event. The patterns in (b), (c) and (d) are all migrated to 200 km depth. Strong multipathing occurs across the whole region, which appears related to the Black Hills structure.

will produce a Δ_{LR} of about 6 s. Thus, these features are distinct and appear to be related to known surface geological features.

Two structures were highlighted; the Cascade Subduction Zone and the Yellowstone Hotspot. Both structures require about the same SH properties, $\Delta_{LR} \sim 6$ s and are accompanied by slow material although the Juan de Fuca slab is continuous with sharp features near Seattle and at the Mendocino Triple Junction. The Yellowstone region produces the most interesting Δ_{LR} patterns. While the Cascade region produces properties associated with the traveltime variation directly with amplitude and Δ_{LR} highly correlated, the Yellowstone data not so much. Although the shallow SRP anomaly is easily seen, there is a small cluster of stations centred on the Idaho–Utah border to the west of Yellowstone that produces strong secondary arrivals only from NW arriving events. Their Δ_{LR} pattern matches that predicted by a narrow plume-like feature, 50 km wide with a 2.5 per cent velocity reduction extending westward into the lower mantle as proposed by Smith *et al.* (2009). To date, we have only worked on teleseismic SH-data and applying this methodology to SV-waveforms will be more difficult because of P–SV interaction (Chu *et al.* 2008). Moreover, the triplication data will help settle the penetration issue.

ACKNOWLEDGMENTS

The authors would like to thank the Editor Christine Thomas and two anonymous reviewers. Their suggestions and comments were greatly appreciated and made significant improvements to the manuscript. Data were provided by IRIS data centers and Earthscope US Array. All maps in this paper were produced using GMT developed by Paul Wessel and Walter H. F. Smith. This work was supported by the Caltech Tectonics Observatory (by the Gordon and Betty Moore Foundation), National Science Foundation (grant 0639507) and contribution #10049 of the Division of Geological and Planetary Science, California Institute of Technology.

REFERENCES

Burdick, L.J. & Helmberger, D.V., 1978. Upper mantle P velocity structure of western United States, *J. geophys. Res.,* **83,** 1699–1712.

Burdick, S. *et al.,* 2008. Upper mantle heterogeneity beneath North America from travel time tomography with global and USArray Transportable Array data, *Seismol. Res. Lett.,* **79**(3), 384–390.

Burdick, S. *et al.,* 2009. Model update December 2008: upper mantle heterogeneity beneath North America from P-wave Travel Time Tomography with Global and USArray Transportable Array Data, *Seismol. Res. Lett.,* **80**(4), 638–645.

Chen, M., Tromp, J., Helmberger, D. & Kanamori, H., 2007. Waveform modeling of the slab beneath Japan, *J. geophys. Res.,* **112,** B2, doi:10.1029/2006JB004394.

Chu, R., Zhu, L., Sun, D. & Helmberger, D.V., 2008. Progress in deriving upper-mantle structure beneath Western U.S., *EOS, Trans. Am. geophys. Un.,* **89**(53), Fall Meet. Suppl., Abstract S33B-1952.

Chu, R.S., Helmberger, D.V., Sun, D., Jackson, J.M. & Zhu L., 2010. Mushy magma beneath Yellowstone, *Geophys. Res. Lett.,* **37,** 1, doi:10.1029/2009GL041656.

Gao, S.S., Liu, K.H., Davis, P.M., Slack, P.D., Zorin, Y.A., Mordvinova, V.V. & Kozhevnikov, V.M., 2003. Evidence for small-scale mantle convection in the upper mantle beneath the Baikal rift zone, *J. geophys. Res.,* **108,** B4, doi:10.1029/2002JB002039.

Gao, W., Grand, S.P., Baldridge, W.S., Wilson, D., West, M., Ni, J.F. & Aster, R., 2004. Upper mantle convection beneath the central Rio Grande rift imaged by P and S wave tomography, *J. geophys. Res.,* **109,** B3, doi:10.1029/2003JB002743.

Ganguly, J., Freed, A.M. & Saxena, S.K., 2009. Density profiles of oceanic slabs and surrounding mantle: integrated thermodynamic and thermal modeling, and implications for the fate of slabs at the 660 km discontinuity, *Phys. of the Earth and Planet. Int.,* **172,** 257–267.

Grand, S.P. & Helmberger D.V., 1984. Upper mantle shear structure of north-America, *Geophys. J. R. astr. Soc.,* **76,** 399–438.

Helmberger, D.V. & Ni S., 2005. Approximate 3D bodywave synthetics for tomographic models, *Bull. seism. Soc. Am.,* **95**(1), 212–224, doi:10.1785/0120040004.

Humphreys, E.D. & Dueker, K.G., 1994. Western United-States uppermantle structure, *J. geophys. Res,.* **99**(B5), 9615–9634.

Humphreys & Eugene D., 1995. Post-Laramide removal of the Farallon slab, western United States, *Geology,* **23**(11), 987–990.

Humphreys, E., Hessler, E., Dueker, K., Farmer, C.L., Erslev, E. & Atwater T., 2003. How Laramide-age hydration of North American lithosphere by the Farallon slab controlled subsequent activity in the western United States, *Int. Geology Rev.,* **45**(7), 575–595.

Jordan, T.H., 1978. Composition and development of continental tectosphere, *Nature,* **274**(5671), 544–548.

Karlstrom, K.E., Whitmeyer, S.J., Dueker, K. & Williams M.L., 2005. Synthesis of results from the CD_ROM experiment: 4-D image of the lithosphere beneath the Rocky Mountains and implications for understanding the evolution of continental lithosphere, in *The Rocky Mountain Region: An Evolving Lithosphere Tectonics, Geochemistry, and Geophysics, Geophys. Monogr. Ser.,* Vol. 154, ed. Karstrom, K.E. & Keller, G.R., AGU, Washington, DC.

King, S.D. & Ritsema, J., 2000. African hot spot volcanism: small-scale convection in the upper mantle beneath cratons, *Science,* **290**(5494), 1137–1140.

Komatitsch, D. & Tromp, J., 2002a. Spectral-element simulations of global seismic wave propagation – I. Validation, *Geophys. J. Int.,* **149**(2), 390–412.

Komatitsch, D. & Tromp, J., 2002b. Spectral-element simulations of global seismic wave propagation – II. Three-dimensional models, oceans, rotation and self-gravitation, *Geophys. J. Int.,* **150**(1), 303–318.

Ni, S.D., Cormier, V.F. & Helmberger, D.V., 2003. A comparison of synthetic seismograms for 2D structures: semianalytical versus numerical, *Bull. seism. Soc. Am.,* **93**(6), 2752–2757, doi:10.1785/0120030011.

Roth, B., Fouch, M.J., James, D.E. & Carlson, R.W., 2008. Three-dimensional seismic velocity structure of the northwestern United States, *Geophys. Res. Lett.,* **35**(15), doi:10.1029/2008GL034669.

Roy, M., Jordan, T.H. & Pederson, J., 2009. Colorado Plateau magnetism and uplift by warming of heterogenous lithosphere, *Nature,* **459,** 978–982.

Schmandt, B., Humphreys, E. & Levander, A., 2009. Multi-scale seismic heterogeneity, complex subduction, and small-scale convection beneath the western U.S., *EOS, Trans. Am. geophys. Un.,* **90**(52), Fall Meet. Suppl., Abstract U23D-0061.

Schmandt, B. & Humphreys, E.D., 2010a. Complex subduction and small-scale convection revealed by body-wave tomography of the western United States upper mantle, *Earth planet. Sci. Lett.,* **297,** 435–445.

Schmandt, B. & Humphreys, E.D., 2010b. Seismically Imaged Relict Slab from the 55 Ma Siletzia Accretion to Northwest USA, *Geology* submitted.

Sigloch, K., McQuarrie, N. & Nolet G., 2006. Measuring finite-frequency body-wave amplitudes and traveltimes, *Geophys. J. Int,* **167,** 271–287.

Sigloch, K., McQuarrie, N. & Nolet G., 2008. Two-stage subduction history under North America inferred from multiple-frequency tomography, *Nature Geosci.,* **1**(7), 458–462.

Smith, K.D., von Seggern, D., Blewitt, G., Preston, L., Anderson, J.G., Wernicke, B.P. & Davis, J.L., 2004. Evidence for deep magma injection beneath Lake Tahoe, Nevada-California, *Science,* **305,** 1277–1280, doi:10.1126/science.1101304.

Smith, R.B. *et al.,* 2009. Geodynamics of the Yellowstone hotspot and mantle plume: seismic and GPS imaging, kinematics, and mantle flow, *J. Volc. Geotherm. Res.,* **188**(1–3), 26–56.

Song, T.R.A. & Helmberger D.V., 2007a. Validating tomographic model with broad-band waveform modelling: an example from the LA RISTRA transect in the southwestern United States, *Geophys. J. Int.,* **171,** 244–258.

Song, T.R.A. & Helmberger D.V., 2007b. P and S waveform modeling of continental sub-lithospheric detachment at the eastern edge of the Rio Grande Rift, *J. geophys. Res.,* **112,** B7, doi:10.1029/2007JB004942.

Song, T.R.A. & Helmberger D.V., 2007c. A depleted, destabilized continental lithosphere near the Rio Grande rift, *Earth planet. Sci. Lett.,* **262,** 175–184.

Sun, D., Helmberger, D., Ni, S. & Bower, D., 2009. Direct measures of lateral velocity variation in the deep Earth, *J. geophys. Res.,* **114,** B05303, doi:10.1029/2008JB005873.

Sun, D., Helmberger, D. & Gurnis M., 2010. A Narrow, Mid-Mantle Plume below Southern Africa, *Geophys. Res. Lett.,* **37,** L09302, doi:10.1029/2009GL042339, in press.

Tan, Y. & Helmberger, D.V., 2007. Trans-Pacific upper mantle shear velocity structure, *J. geophys. Res.,* **112,** B8, doi:10.1029/2006JB004853.

Tian, Y., Sigloch, K. & Nolet, G., 2009. Multiple-frequency SH-wave tomography of the western US upper mantle, *Geophys. J. Int.,* **178,** 1384–1402, doi:10.1111/j.1365-246X. 2009.04225.x.

Vidale, J., 1988. Finite-difference calculation of travel-times, *Bull. seism. Soc. Am.,* **78**(6), 2062–2076.

Waite, G.P., Smith, R.B. & Allen R.M., 2006. V-P and V-S structure of the Yellowstone hot spot from teleseismic tomography: evidence for an upper mantle plume, *J. geophys. Res.,* **111,** B4, doi:10.1029/2005JB003867.

Xue, M. & Allen, R.M., 2007. The Fate of the Juan de Fuca Plate: implications for a Yellowstone Plume Head, *Earth planet. Sci. Lett.,* **264**(1–2), 266–276, doi:10.1016/j.epsl.2007.09.04.

Xue, M. & Allen R.M., 2010. Mantle structure beneath the Western US and its implications for convection processes, *J. geophys. Res.,* **115,** B07303, doi:10.1029/2008JB006079.

Yang, Y., Ritzwoller, M.H., Lin, F.-C., Moschetti, M.P. & Shapiro N.M., 2008. Structure of the crust and uppermost mantle beneath the western United States revealed by ambient noise and earthquake tomography, *J. geophys. Res.,* **113,** B12310, doi:10.1029/2008JB005833.